Extension of Traditional Beamforming Methods to the Continuous-Scan Paradigm

David Morata* and Dimitri Papamoschou.†
University of California, Irvine, Irvine, CA, 92607

The paper adapts the delay-and-sum beamforming method and associated deconvolution techniques for microphone measurements that comprise fixed and continuously-scanning sensors. The signals from the scanning sensors are non-stationary due to the traversing of a spatially-varying acoustic field. Quasi-stationarity is sought by dividing the signals into smaller blocks and applying a frequency-dependent window within each block. In addition, the motion of the sensors requires a modification to the steering vectors to include a Doppler-shifted frequency. Three distinct methods are used to generate the noise source maps. The first is a natural extension of the delay-and-sum process for continuously-scanning microphone arrays. The source image is obtained by using the distinct contributions from the cross-spectral matrices for each block. This technique shows a suppressed level of the sidelobes and an increased spatial resolution compared to the use of delay-and-sum with fixed sensors. Two additional processes are presented and adapted to the continuous-scan paradigm with the aim of constructing a global cross-spectral matrix that is representative of the complete experimental run. The global cross-spectral matrix is obtained with partial-fields decomposition and a cross-spectral matrix completion technique. These two methods show a higher suppression of the sidelobes compared to the first. All three techniques yield highly-resolved noise source maps of similar quality, attaining very high spatial resolutions. Advanced beamforming and deconvolution techniques are used to further enhance the spatial resolution of the noise source. The techniques are first applied to the imaging of a synthetic distributed source to assess their performance. The methods are then used to obtain the noise source distribution of an imperfectly-expanded supersonic jet that presented the phenomenon of screech. It is demonstrated that any of the methodologies introduced allows the resolution of the shock cells in the jet plume.

I. Nomenclature

D	=	jet diameter
$\mathbf{e}$	=	steering vector
f	=	cyclic frequency
$\mathbf{G}$	=	Cross Spectral Matrix
$\mathcal{M}$	=	number of microphones
$\mathcal{N}_x$	=	number of divisions of the region of interest
N_{FFT}	=	size of Fast Fourier Transform
P_m	=	Fourier Transform of $p_m(t)$
r	=	iteration step
R	=	residual error
S	=	Point Spread Function
T	=	block length in seconds
t	=	time
U	=	fully-expanded jet velocity
V	=	sensor speed
w_m, W_m	=	weights of microphone m
x	=	axial coordinate
y	=	transverse coordinate

*Graduate Student Researcher, Mechanical and Aerospace Engineering, dmoratac@uci.edu, Member AIAA.
†Professor, Mechanical and Aerospace Engineering, dpapamos@uci.edu, Fellow AIAA.

Y	=	array power output
α	=	derivative of Eq. 8
θ	=	polar angle relative to jet axis
λ	=	acoustic wavelength
ℓ	=	source-sensor distance
τ	=	source-sensor travel time
ξ	=	coordinate along the region of interest
ω	=	angular frequency
ω'	=	Doppler-shifted frequency

Subscripts

k	=	block index
m	=	microphone index
n	=	microphone index
s	=	scanning sensor
f	=	fixed sensor

Acronyms

CSDAS	=	Continuous-Scan Delay-And-Sum
CSM	=	Cross-Spectral Matrix
CSMC	=	Cross-Spectral Matrix Completion
DAS	=	Delay-And-Sum
FFT	=	Fast Fourier Transform
PF	=	Partial Fields
PSF	=	Point Spread Function
R-L	=	Richardson-Lucy
SPL	=	Sound Pressure Level

II. Introduction

Beamforming has become an industry standard to investigate the noise generated by aeroacoustic sources. Traditional beamforming techniques use the signals from fixed microphones to construct the Cross-Spectral Matrix (CSM). The noise source images are obtained by "steering" the CSM to the region of interest using the steering vectors. This is done by delaying (or phasing), summing and normalizing microphone signals that have been simultaneously acquired. This is at the heart of the well known delay-and-sum (DAS) technique [1, 2]. The approach requires previous knowledge of the wave propagation velocity, the speed of sound, and the positions of the microphones relative to the location of the area where significant noise sources are expected.

One of the drawbacks of the DAS algorithm is that its spatial resolution is, in many instances, not high enough for aeroacustic applications of interest. To enhance its resolution, one can consider increasing the number of closely-spaced sensors of the array in order to mitigate the effects of the array point spread function, thus reducing the sidelobes. In addition, the array aperture can also be increased to reduce the main lobe beamwidth and improve the array spatial resolution. However, the process of increasing the number of microphones is expensive and not viable in most applications, and increasing the array aperture might be detrimental in certain conditions involving directional noise sources, such as jet noise. In an effort to enhance the spatial resolution obtained with traditional beamforming, past research has considered shading algorithms and non-uniform microphone weightings [1, 3]. These techniques attenuate the effect of the sidelobes up to a certain level but the resulting image might not still have the desired resolution. The effect of the sidelobes can be further mitigated by using a deconvolution approach. Such approaches have been widely investigated in the past [3–7] and typically assume a certain nature about the noise source (e.g. uncorrelated monopoles). The goal of such techniques is to separate the contribution of the point spread function from the imaged source distribution.

Recently there has been an increasing interest in arrays that contain fixed and continuously-scanning sensors. The method is an extension of the stop-and-start process of Ref. [8] used in Near-Field Acoustic Holography (NAH).

The continuous-scan paradigm has been shown to improve the spatial resolution of the noise source maps for a fixed sensor count [9], and recently found applications in order tracking [10], NAH [11], and beamforming [9, 12, 13]. The methodology has been shown to be ideal for budget microphone arrays, where their geometrical properties are highly constrained by the low number of sensors used. Additionally, the continuous-scan approach reduces the total acquisition time by an order of magnitude compared to utilizing fixed sensors only [14]. However, care must be taken in the processing of the signals from continuous-scan phased arrays. The motion of the sensors introduces non-stationarity in the signal statistics due the variation of the source-sensor distance and the possibility of traversing of a spatially-varying acoustic field, such as that emitted by subsonic and supersonic jets. Ref. [9] performed a detailed analysis of the non-stationarity and used the Wigner-Ville spectrum to quantify its effects. Suppression of the signal non-stationarity involved the division of the signal into quasi-stationary blocks and the application of a frequency-dependent window within each block.

This work introduces three methods to process pressure signals from microphone arrays containing continuously-scanning sensors for beamforming applications. The first method is a natural extension of the DAS process for arrays that contain continuously-scanning sensors. Accordingly, the steps involved in the fixed-reference DAS process are first described and then adapted to the continuous-scan paradigm. A drawback of this first approach is the lack of a global cross-spectral matrix that is representative of the complete experiment run. Thus, two additional methodologies are presented with the aim at constructing a global CSM. These two methods involve a cross-spectral matrix completion process and a partial fields decomposition technique. The three techniques show highly-resolved noise source maps of similar quality, with almost complete suppression of the sidelobes. A few deconvolution techniques are used to further sharpen the noise source maps. The methodologies are first applied to a synthetic noise source to evaluate the performance of the different continuous-scan methods. Then, a supersonic underexpanded jet that presented the phenomenpn of screech is investigated. This aeroacoustic source is of interest given its intricate flow field containing shock cells in combination with large and fine scale turbulence structures interacting with them and creating additional noise sources.

The paper is structured as follows: the steps involved in traditional beamforming are first introduced. This methodology is extended to phased arrays that comprise fixed and continuously-scanning sensors. Then, two distinct methods, including a cross-spectral matrix completion (CSMC) and partial fields decomposition (PF) are introduced to construct a global CSM that is representative of the full experiment. The experimental setup is briefly described next, including the microphone array and the noise sources of interest. The results and conclusions sections follow.

III. Methodology

A. Continuous-Scan Delay-And-Sum Beamforming

1. Introduction

In frequency domain, the starting point in traditional beamforming is the computation of the cross-spectral matrix (CSM). Each element of the CSM is the auto- or cross-spectral density of microphone signals $p_m(t)$ and $p_n(t)$. The CSM for a frequency ω is thus defined as

$$\mathbf{G}(\omega) = G_{mn}(\omega) = \overline{P_m(\omega)P_n^*(\omega)} \tag{1}$$

where m and n are the microphone indexes, P_m and P_n are the Fourier transforms of $p_m(t)$ and $p_n(t)$, and $*$ denotes the complex conjugate. The symbol $\overline{(\cdot)}$ is used to indicate the ensemble average involved in the Fast Fourier Transform algorithm. The size of the CSM is $\mathcal{M}_f \times \mathcal{M}_f$, where $\mathcal{M}_f$ is the total number of fixed microphones used.

The CSM is "steered" to the region of interest using steering vectors. In the modeling presented here it is assumed that the medium has a constant speed of sound a_∞ and the source comprises uncorrelated point sources distributed linearly (see Fig. 1), which is the standard used in many beamforming algorithms. For fixed sensors, the steering-vector element associated with microphone m and steering location ξ is

$$e_m(\xi, \omega) = w_m \exp(i\omega\tau_m(\xi)) \tag{2}$$

where w_m is a microphone weight and $\tau_m(\xi)$ is the source-sensor travel time

$$\tau_m(\xi) = \frac{\ell_m(\xi)}{a_\infty} \tag{3}$$

The w_m term may include corrections for sound convected and refracted through the shear layer to each microphone [15, 16]. The steering vector to location ξ is denoted by $\boldsymbol{e}(\xi, \omega)$, and has dimensions of $1 \times \mathcal{M}_f$.

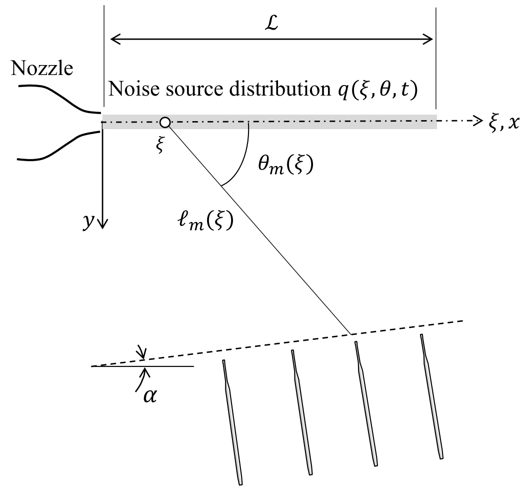

Fig. 1 Line source distribution and far-field microphone array containing only fixed microphones.

The goal of traditional beamforming methods is to obtain the array power spectrum, which gives information about the distribution and intensity of the noise sources within the region of interest. The array power spectrum at location ξ is defined as

$$Y(\xi, \omega) = \frac{\mathbf{e}(\xi, \omega)\ \mathbf{G}(\omega)\ \mathbf{e}^H(\xi, \omega)}{\mathcal{M}_f^2} \tag{4}$$

where H denotes the complex transpose. Equation 4 results from introducing a time delay $\tau_m(\xi)$ to each microphone signal, summing the signals, and taking the Fourier transform of the sum, in a process known as delay-and-sum (DAS) beamforming.

A modified version of Eq. 4 can be used to improve the dynamic range of the array, removing the microphone self-noise contamination and giving more weight to the cross-spectral terms, which provide phase information about the source. Assuming the microphone noise contamination to be concentrated along the CSM diagonal, it is a standard procedure to compute beamformed maps as

$$Y(\xi, \omega) = \frac{\mathbf{e}(\xi, \omega)\ \mathbf{G}_{\text{diag=0}}(\omega)\ \mathbf{e}^H(\xi, \omega)}{\mathcal{M}_f^2 - \mathcal{M}_f} \tag{5}$$

where $\mathbf{G}_{\text{diag=0}}(\omega)$ places zeros on the diagonal of the CSM. However, one must be careful when performing the diagonal removal operation as the resulting CSM might contain negative eigenvalues, associated with negative source auto-powers, which are deemed to be non-physical. An alternative approach to the diagonal removal method is the diagonal reconstruction method (DiRec) of Hald [17] or that of Dougherty [18]. The DiRec method can be understood as a semidefinite programming (SDP) problem, thus allowing the use of powerful convex optimization libraries such as CVX. If such approach is used, the resulting beamformed image can be obtained with Eq. 4 using the CSM with the optimized diagonal.

2. Array Power Spectrum with Continuously Scanning Sensors

We consider $\mathcal{M}_f$ fixed sensors and $\mathcal{M}_s$ scanning sensors. In extending the DAS methodology to continuously-scanning sensors, we follow the usual summation method but with time delays that are time-dependent:

$$s(\xi, t) = \sum_{m=1}^{\mathcal{M}_f+\mathcal{M}_s} w_m p_m(t + \tau_m(\xi, t)) \tag{6}$$

The source-sensor time is $\tau_m(\xi,t) = \ell_m(\xi,t)/a_\infty$. For a scanning sensor, the signal $p_m(t)$ is non-stationary due to the time-varying source-sensor distance and statistical inhomogeneity of the traversed acoustic field. Quasi-stationarity is sought by dividing the signal into a number of overlapping or non-overlapping blocks of duration T (see Fig. 2) , similar to Ref. [9]. A first-order Taylor series expansion is used to approximate the source-sensor travel time for each block k

$$\tau_m(\xi,t) \approx \tau_{mk}(\xi) + \left.\frac{\partial \tau_m(\xi,t)}{\partial t}\right|_{t=t_k} (t - t_k) \tag{7}$$

where t_k is the center time of the block and $\tau_{mk}(\xi)$ is the source-sensor travel time calculated from the spatial center of the block. It can be shown that for a microphone array similar to that depicted in Fig. 3

$$\left.\frac{\partial \tau_m(\xi,t)}{\partial t}\right|_{t=t_k} = \frac{V_{mk}}{a_\infty}\frac{(x_{mk}-\xi)\cos\alpha - y_{mk}\sin\alpha}{\ell_{mk}} = \alpha_{mk}(\xi) \tag{8}$$

where V_{mk} is the velocity of scanning sensor m for block k, thus allowing for the possibility of position-dependent sensor speeds.

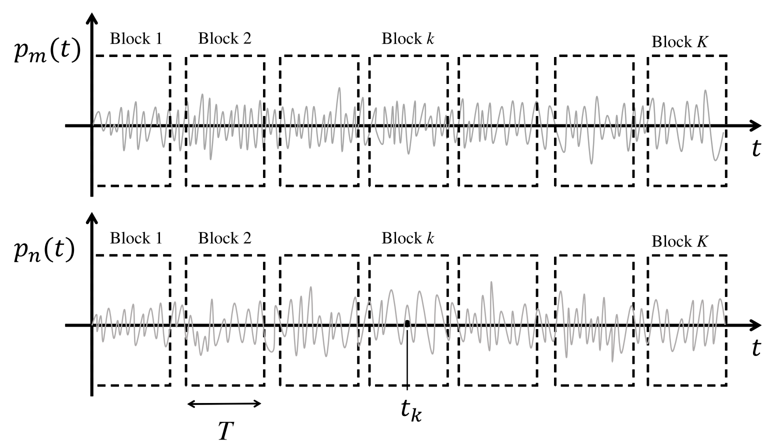

Fig. 2 Illustration of the division of the signal into K quasi-stationary blocks without block overlap.

Equation 6 is now approximated as

$$s_k(\xi,t) = \sum_{m=1}^{\mathcal{M}_f+\mathcal{M}_s} w_{mk} p_{mk}[(1+\alpha_{mk}(\xi))t + \tau_{mk}(\xi)] \tag{9}$$

where $p_{mk}(t)$ is the pressure recorded by sensor m at block k. Its Fourier transform is

$$P_{mk}(\omega) = \int_{-\infty}^{\infty} p_{mk}(t) e^{-i\omega t} dt \tag{10}$$

The Fourier Transform of the summation of all the microphone signals for block k is

$$\begin{aligned} S_k(\xi,\omega) &= \int_{-\infty}^{\infty} \sum_{m=1}^{\mathcal{M}_f+\mathcal{M}_s} w_{mk}\ p_{mk}[(1+\alpha_{mk}(\xi))t + \tau_{mk}(\xi)]\ e^{-i\omega t} dt \\ &= \sum_{m=1}^{\mathcal{M}_f+\mathcal{M}_s} \frac{w_{mk}}{1+\alpha_{mk}(\xi)} P_{mk}(\omega'_{mk}(\xi))\ e^{i\omega'_{mk}\tau_{mk}(\xi)} \end{aligned} \tag{11}$$

where $\omega'_{mk}(\xi)$ is the Doppler-shifted frequency of Ref. [9], given by

$$\omega'_{mk}(\xi) = \frac{\omega}{1+\alpha_{mk}(\xi)} \tag{12}$$

For low scan Mach number (i.e. $V_{mk}/a_\infty << 1$), the Fourier transform of the pressure signal $P_{mk}(\omega'_{mk})$ can be approximated as $P_{mk}(\omega)$ with little error. On defining

$$W_{mk}(\xi) = \frac{w_{mk}}{1 + \alpha_{mk}(\xi)} \tag{13}$$

the Fourier Transform of the summation of all microphone signals for block k is rewritten as

$$S_k(\xi, \omega) = \sum_{m=1}^{\mathcal{M}_f + \mathcal{M}_s} W_{mk}(\xi)\ P_{mk}(\omega)\ e^{i\omega'_{mk}\tau_{mk}(\xi)} \tag{14}$$

The non-normalized array output for block k is

$$Y_k(\xi, \omega) = \sum_{m=1}^{\mathcal{M}_f + \mathcal{M}_s} \sum_{n=1}^{\mathcal{M}_f + \mathcal{M}_s} W_{mk}(\xi) W_{nk}(\xi)\ \overline{P_{mk}(\omega) P^*_{nk}(\omega)}\ e^{i\omega'_{mk}(\xi)\tau_{mk}(\xi)}\ e^{-i\omega'_{nk}(\xi)\tau_{nk}(\xi)} \tag{15}$$

Defining the CSM for block k as

$$\mathbf{G}_k(\omega) = \overline{P_{mk}(\omega) P^*_{nk}(\omega)} \tag{16}$$

with a size of $(\mathcal{M}_f + \mathcal{M}_s) \times (\mathcal{M}_f + \mathcal{M}_s)$, the array output for block k is calculated as

$$Y_k(\xi, \omega) = \mathbf{e}_k(\xi, \omega)\ \mathbf{G}_k(\omega)\ \mathbf{e}^H_k(\xi, \omega) \tag{17}$$

where

$$\mathbf{e}_k(\xi, \omega)\ =\ e_{mk}(\xi, \omega)\ =\ W_{mk} e^{i\omega'_{mk}(\xi)\tau_{mk}(\xi)} \tag{18}$$

is the modified steering vector used in the continuous-scan delay-and-sum (CSDAS) beamforming approach, with size $1 \times (\mathcal{M}_f + \mathcal{M}_s)$. It can be seen how Eq. 17 bears some similarities to the traditional beamforming expression (Eq. 4). The equation can be modified to remove the microphone self-noise contamination as

$$Y_k(\xi, \omega) = \mathbf{e}_k(\xi, \omega)\ \mathbf{G}_{\text{diag}=0,k}(\omega)\ \mathbf{e}^H_k(\xi, \omega) \tag{19}$$

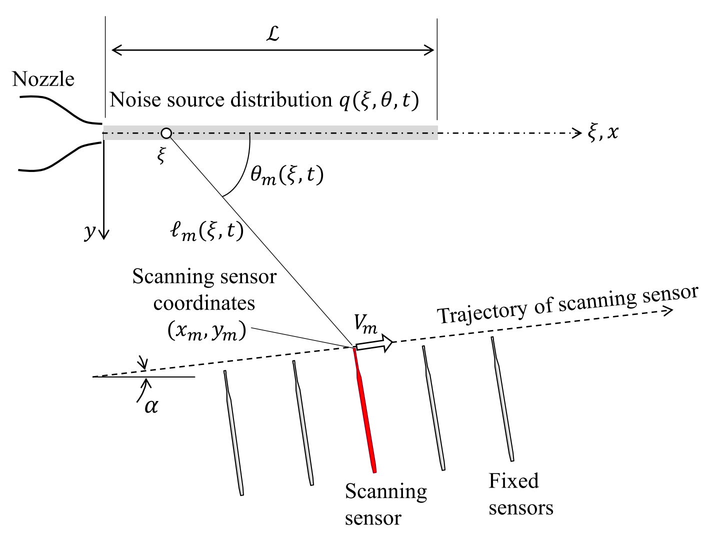

Fig. 3 Line source distribution and far-field microphone array containing fixed microphones and one scanning sensor.

However, one should bear in mind the cautionary note mentioned earlier. The elements of the steering vector of Eq. 18 can be approximated using Eq. 2 with little loss in accuracy. The approximation is reasonable as long as $\omega'_{mk} \approx \omega$.

In other words, the approximation can be used if the fixed and scanning sensors are located in the acoustic far-field, and the scan speed is much lower than the speed of sound (i.e. $V_{mk/a_\infty} << 1$). In this study, $V_{mk/a_\infty} = 0.0002$. If using such approach, the scanning microphone position is assumed to be the center of the block.

In calculating the auto- and cross-spectral densities of Eq. 16, care must be taken when handling non-stationary signals. As outlined in Ref. [9], the most important manifestation of the non-stationarity of the signal is on the cross-correlations of sensors that have a relative velocity. Considering only one sensor scanning with speed V_μ, minimization of the non-stationarity effects entails selection of a block size such that

$$V_\mu T << \lambda \tag{20}$$

where λ is the acoustic wavelength. The relationship implies that the block size must be reduced as the frequency resolved increases. However, it is not feasible to select a block duration for each wavelength, as the cost of obtaining the noise source maps would be prohibitive. Instead, Ref. [9] proposed to use a frequency-dependent window that shortens the block size dynamically. Ref. [9] used an energy-conserving Gaussian window, with the energy-conserving requirement formulated as

$$\int_{-T/2}^{T/2} |g(\omega,t)|^2 dt = T \tag{21}$$

where $g(\omega,t)$ is the frequency-dependent function. Besides the Gaussian window of Ref. [9], two additional functions were used in this work: a hyperbolic secant and a Cauchy distribution. The results were largely independent of the function, hence only the results computed with the Gaussian window have been included. However, the expressions for the windows are given in Table 1 for completeness. All windows are of the form

$$g(\omega,t) = A(\omega) f(\omega,t) \tag{22}$$

where $f(\omega,t)$ denotes the shape of the window and $A(\omega)$ is a parameter to ensure fulfillment of Eq. 21.

	$A(\omega)$	$f(\omega,t)$
Gaussian	$\left(\frac{2}{\pi}\right)^{1/4}\sqrt{\frac{T}{\delta(\omega)}\frac{1}{\text{erf}\frac{T}{\sqrt{2}\delta(\omega)}}}$	$\exp\left[-\left(\frac{t}{\delta(\omega)}\right)^2\right]$
Hyperbolic Secant	$\sqrt{\frac{k(\omega)T}{2\tanh(k(\omega)T/2)}}$	$\text{sech}(k(\omega)T)$
Cauchy distribution	$\sqrt{1/\left(\frac{2}{(\sqrt{k(\omega)}T)^2+4}+\frac{\tan^{-1}(\sqrt{k(\omega)}T/2)}{\sqrt{k(\omega)}T}\right)}$	$\frac{1}{k(\omega)t^2+1}$

Table 1 Expressions for the frequency-dependent windows.

The tuning parameters are $\delta(\omega)$ for the Gaussian window and $k(\omega)$ for the rest. The size of the window width $\delta(\omega)$ for the Gaussian function was selected such that [9]

$$V_\mu \delta = c_\lambda \lambda \tag{23}$$

where c_λ is the fraction of the wavelength traversed by the scanning sensor with time δ. The parameter $k(\omega)$ represents the number of wavelengths λ traversed by a scanning sensor with velocity V_μ for block duration T, and was selected such that $k(\omega) \sim V_\mu/a_\infty T 2\pi\omega$. The frequency-dependent window was implemented in conjunction with the calculations of the auto- and cross-spectral densities (Eq. 16), and only applied to the CSM elements that involved the scanning sensor. The reader is referred to Ref. [9] for a detailed description of the Gaussian window and its implementation.

3. Overall Array Response

Equation 17 gives the array response for a given block k. In assembling the responses over all the blocks, care must be taken to include only the distinct elements of the CSMs (Eq. 16) as to avoid averaging of repeated information. The

CSM for the first block, Block 0, comprises the signals of the fixed sensors only. Given that only stationary signals are processed, the CSM for Block 0 uses the entire duration of the signals. For the blocks $k = 1, 2, ..., K$ only the contributions from the scanning sensors are used. These contributions can be considered as additional information from "virtual microphones", the coordinates of which are at the center of the block k. The process is illustrated in Fig. 4, where two microphones are scanning (sensors 1-2) and five are fixed (sensors 3 - 7). The contribution from the fixed sensors is highlighted in blue while the terms involving scanning sensors are highlighted in green. Only the bold elements are used to produce the noise source map for each block.

Block 0

1,1	1,2	1,3	1,4	1,5	1,6	1,7
2,1	2,2	2,3	2,4	2,5	2,6	2,7
3,1	3,2	**3,3**	**3,4**	**3,5**	**3,6**	**3,7**
4,1	4,2	**4,3**	**4,4**	**4,5**	**4,6**	**4,7**
5,1	5,2	**5,3**	**5,4**	**5,5**	**5,6**	**5,7**
6,1	6,2	**6,3**	**6,4**	**6,5**	**6,6**	**6,7**
7,1	7,2	**7,3**	**7,4**	**7,5**	**7,6**	**7,7**

Block 1

1,1	**1,2**	**1,3**	**1,4**	**1,5**	**1,6**	**1,7**
2,1	**2,2**	**2,3**	**2,4**	**2,5**	**2,6**	**2,7**
3,1	**3,2**	3,3	3,4	3,5	3,6	3,7
4,1	**4,2**	4,3	4,4	4,5	4,6	4,7
5,1	**5,2**	5,3	5,4	5,5	5,6	5,7
6,1	**6,2**	6,3	6,4	6,5	6,6	6,7
7,1	**7,2**	7,3	7,4	7,5	7,6	7,7

…

Block K

1,1	**1,2**	**1,3**	**1,4**	**1,5**	**1,6**	**1,7**
2,1	**2,2**	**2,3**	**2,4**	**2,5**	**2,6**	**2,7**
3,1	**3,2**	3,3	3,4	3,5	3,6	3,7
4,1	**4,2**	4,3	4,4	4,5	4,6	4,7
5,1	**5,2**	5,3	5,4	5,5	5,6	5,7
6,1	**6,2**	6,3	6,4	6,5	6,6	6,7
7,1	**7,2**	7,3	7,4	7,5	7,6	7,7

Fig. 4 Distinct elements of the Cross Spectral Matrices for an array with two microphones scanning (1 and 2) and five microphones fixed (3 to 7). Highlighted in green are the terms that involve the scanning sensors and in blue the terms that involve the fixed sensors. The bold font indicates the elements used to compute the noise source map for a given block.

It is easy to show that the number of elements used to compute the noise source map is then

$$J = (\mathcal{M}_f - \mathcal{M}_s)^2 + (K - 1)\mathcal{M}_s(2\mathcal{M}_f - \mathcal{M}_s) \tag{24}$$

When the diagonal is removed from the CSM, the number of elements is

$$J = (\mathcal{M}_f - \mathcal{M}_s)^2 - (\mathcal{M}_f - \mathcal{M}_s) + (K - 1)\mathcal{M}_s(2\mathcal{M}_f - \mathcal{M}_s - 1) \tag{25}$$

Note that if the DiRec method is used to mitigate the microphone self-noise contamination on a block by block basis, the number of total elements is that of Eq. 24. The noise source maps are constructed by summing the contributions from all blocks and normalizing by the number of elements used as

$$Y(\xi, \omega) = \frac{1}{J} \sum_{k=0}^{K} Y_k(\xi, \omega) \tag{26}$$

Inserting Eq. 17,

$$Y(\xi, \omega) = \frac{1}{J} \sum_{k=0}^{K} \mathbf{e}_k(\xi, \omega)\ \mathbf{G}_k(\omega)\ \mathbf{e}_k^H(\xi, \omega) \tag{27}$$

The equation constitutes the extension of the delay-and-sum methodology to the continuous-scan paradigm (CSDAS).

B. Cross-Spectral Matrix Completion

One drawback of the previously introduced approach is the lack of a global CSM. The noise source distribution is computed using only the distinct elements of the CSM obtained for every block. This complicates the use of advanced beamforming and deconvolution techniques, as many of these are based on a global CSM [7, 19]. The need for constructing a CSM that is representative of the complete experiment run becomes evident.

During the past several years, research on noise source localization using a collection of non-synchronous microphone measurements has gained momentum [20–24]. An initial approach consisted in moving a prototype array sequentially. However, the phase relationships between the microphones of the array at two distinct sequential positions were lost, thus resulting in a penalization in the spatial resolution needed for beamforming applications. To overcome the problem, a strategy consisting in placing reference microphones near the source was later employed. Such microphones were used to recover the missing phase relationships between consecutive positions of the array by conditioned spectral analysis and principal component analysis [25] in a procedure similar to the partial fields decomposition presented in Section III.C. However, in order for the missing phase relationships to be sufficiently well resolved, a high number of reference sensors were usually needed to capture the number of uncorrelated noise sources, yielding a prohibitive cost for certain applications.

A novel approach to finding the missing phase relationships of sequential microphone measurements was formulated in Refs. [25, 26]. The idea behind the methodology was the completion of the CSM obtained from non-synchronous microphone arrays (i.e. the estimation of the missing entries of a sparse CSM). The methodology has been successfully applied in the past to simulated and simple speaker sources [26], as well as some industrial devices [27]. This section introduces a way to obtain a global CSM that bears similarities to the spectral matrix reconstruction of Ref. [26]. The methodology is extended to the continuous-scan paradigm, thus reducing the total experimental time significantly [14] compared to sequential measurements, and applied to the imaging of underexpanded jets. Other approaches were also explored but were unsuccessful. Specifically, a methodology similar to the array interpolation approach of Ref. [28] was tested; however, the spatial distribution of the noise sources at high frequency was relatively poor, due to the phase unwrapping not being perfectly linear.

The CSM completion approach is usually formulated as a matrix rank minimization problem (low rank model) subject to some constraints. However, as discussed by Yu [29], estimating the rank of a matrix can be cumbersome when dealing with signals produced by a high number of uncorrelated sources, and when working with signals that involve moderate to high levels of noise in the measurements. In addition, the rank minimization approach involves setting an experimentally-found thresholding parameter to find the most relevant eigenvalues associated to the number of uncorrelated acoustic sources, yielding to a higher degree of variability of the results. Thus, the low rank model is usually reformulated as a weakly sparse eigenvalue spectrum problem. This enables the use of advanced semidefinite programming (SDP) algorithms and libraries used in convex optimization applications. Instead of imposing a reduced fixed rank, the completed CSM is of full rank and contains a few dominant eigenvalues. The problem then results in minimizing the nuclear norm of the global CSM subject to some constraints. The nuclear norm of the global CSM is defined as

$$\|\mathbf{G}_C(\omega)\|_* = \sum_{i=1}^{\mathcal{M}_f+K\mathcal{M}_s} \lambda_i^2(\omega) \tag{28}$$

where λ_i are the eigenvalues. The full CSM $\mathbf{G}_C$ contains the contributions from fixed and scanning microphones, and has a size of $(\mathcal{M}_f + K\mathcal{M}_s) \times (\mathcal{M}_f + K\mathcal{M}_s)$. The constraints needed to establish a unique and physical solution to the problem are described next.

The first restrictions imposed on the global CSM are the Hermitian and semipositive definite conditions. That is

$$\mathbf{G}_C(\omega) = \mathbf{G}_C^H(\omega) \tag{29}$$

and

$$\mathbf{G}_C(\omega) \geq 0 \tag{30}$$

respectively. This ensures that there are no negative eigenvalues associated with negative source auto-spectral densities. Next, a condition is imposed such that the completed CSM does not change the existing measured entries of the sparse CSM, denoted by $\mathbf{G}_S$. This requirement is relaxed and stated as

$$\|\mathcal{A}(\mathbf{G}_C(\omega)) - \mathbf{G}_S(\omega)\|_F \leq \epsilon_1 \tag{31}$$

where the $\mathcal{A}(\cdot)$ operator extracts the positions containing only the measured cross- and auto-spectral densities of the sparse CSM, $\|\cdot\|_F$ is the Frobenius norm, and ϵ_1 is a thresholding error that relaxes the constraint.

A global CSM for the complete experiment run can be calculated using the above requirements. However, the solution might not be unique and might not be necessarily physical. Thus, a new constraint is included to obtain physical results. The new constraint ensures the continuity of the acoustic far-field [29] by using a smoothing operator that encodes the positions of the microphones, fixed and scanning (i.e. the center of the blocks). The operator acts as a filter on the global CSM, preventing significant variations between the auto- and cross-spectral densities of microphones pairs that are very close. The filter is denoted by $\mathbf{\Psi}$ and is constructed using a dimension-reduced Fourier spatial basis

$$\mathbf{\Theta} = \exp\left[i(k_x\mathbf{x} + k_y\mathbf{y})\right] \tag{32}$$

where $\mathbf{x}$ and $\mathbf{y}$ represent the coordinates of the fixed sensors and center coordinates of the blocks, and (k_x, k_y) are spatial wavenumbers. Following the guidance of Yu *et al.* [26], the wavenumbers are discretized as $k_x^n = n\Delta k_x$, with $n = -N, ..., N$, and similarly for k_y, with $k_y^m = m\Delta k_y$ and $m = -M, ..., M$. The expressions for k_y will be obviated in the analysis that follows, given their similarity to those obtained for k_x. The maximum spatial frequency is $k_{x,\max} = N\Delta k_x = \frac{\pi}{\Delta x}$. The spatial frequency can be related to the array aperture as $\Delta k_x = \frac{2\pi}{L_x}$. Here, we assume that the acoustic waves will not change significantly within the small Δz offset between the fixed and scanning microphones (see Section IV.B); hence we have not included the third dimension in our formulation. However, the methodology can be extended for sensors with greater Δz offsets. The choice of the above spatial basis is valid as long as the far-field correlation length ℓ_c is larger than the average distance between two microphones or block centers. A general rule to determine the minimum resolution of the dimension-reduced basis is $\Delta x, \Delta y \geq \min(\ell_c, 2d_c)$, where d_c represents the distance between two contiguous microphones or block centers. In this study, we used $\Delta x = \Delta y = 6$ mm, with $d_c \approx 4.8$ mm and assuming $l_c < 6$ mm at the highest frequencies that were resolved.

Then, the smoothing filter is constructed as

$$\boldsymbol{\Psi} = \boldsymbol{\Theta}\boldsymbol{\Theta}^\dagger \tag{33}$$

where $\boldsymbol{\Theta}^\dagger$ is the pseudo-inverse, which is found using the Moore-Penrose method. The Moore-Penrose inverse is defined as $\boldsymbol{\Theta}^\dagger = \mathbf{V}\boldsymbol{\Sigma}^{-1}\mathbf{U}^{\mathbf{H}}$, where the rectangular diagonal matrix $\boldsymbol{\Sigma}^{-1}$ is

$$\boldsymbol{\Sigma}^{-1} = \begin{pmatrix} \sigma_{11}^{-1} & 0 & \cdots & 0 \\ 0 & \sigma_{22}^{-1} & \cdots & 0 \\ \vdots & \vdots & \ddots & \vdots \\ 0 & 0 & \cdots & \sigma_{2N\times 2M}^{-1} \end{pmatrix} \tag{34}$$

and contains non-negative numbers only; $\boldsymbol{\Theta} = \mathbf{U}\boldsymbol{\Sigma}\mathbf{V}^{\mathbf{H}}$ is the singular value decomposition of the matrix, where $\mathbf{V}$ and $\mathbf{U}$ are the singular value vector matrices; and $\boldsymbol{\Sigma}$ is a rectangular diagonal matrix containing the singular values. Note that M and N do not necessarily need to be equal, as they depend on the discretization used to obtain the reduced-dimension spatial basis. Obviously, the entries of the CSM must not be significantly changed as a consequence of the filtering, a requirement that is expressed as

$$\|\boldsymbol{\Psi}\mathbf{G}_C(\omega)\boldsymbol{\Psi}^{\mathbf{H}} - \mathbf{G}_C(\omega)\|_F \leq \epsilon_2 \tag{35}$$

where ϵ_2 is a thresholding error. Having introduced all the required variables, the problem of CSM completion for continuous-scan phased arrays is formulated as

$$\begin{aligned} \text{minimize} \quad & \|\mathbf{G}_C(\omega)\|_* \\ \text{subject to} \quad & \|\mathcal{A}(\mathbf{G}_C(\omega)) - \mathbf{G}_S(\omega)\|_F \leq \epsilon_1 \\ & \|\boldsymbol{\Psi}\mathbf{G}_C(\omega)\boldsymbol{\Psi}^{\mathbf{H}} - \mathbf{G}_C(\omega)\|_F \leq \epsilon_2 \\ & \mathbf{G}_C(\omega) = \mathbf{G}_C^H(\omega) \geq 0 \end{aligned} \tag{36}$$

The above methodology has been successfully applied to block-Hermitian matrix completion problems in past beamforming studies [20–22, 26, 27, 29]. However, a key difference is that the sparse CSM $\mathbf{G}_S$ obtained in the context of the continuous-scan paradigm is not in general block-Hermitian. The global CSM is obtained, as per Eq. 36, using the Fast Iterative Shrinkage Thresholding Algorithm (FISTA) approach of Ref. [27].

Figure 5 shows an example of the sparse CSM obtained during a continuous-scan experiment with one moving sensor. The contributions from the fixed sensors, denoted by 1, 2 and 3, are marked in blue, while the contribution from one scanning sensor (i.e. the different blocks), denoted by S, is marked in green. The missing relationships correspond to the cross-spectral densities between two distinct blocks, and are left blank in the figure. To aid the visualization and allow for a correct sorting of the steering vectors to find the array power spectrum, the elements of the global CSM are sorted from low to high polar angles in this work. In addition, when the scanning sensor is involved, the corresponding auto- and cross-spectral densities are computed with the frequency-dependent window introduced in the previous section, as outlined in Ref. [9]. This ensures that the non-stationarity in the sensor's cross-correlations is suppressed.

The completed CSM is steered to location ξ within the region of interest to find the array power spectrum as

$$Y(\xi, \omega) = \frac{\mathbf{e}(\xi, \omega)\mathbf{G}_C(\omega)\mathbf{e}^H(\xi, \omega)}{J} \tag{37}$$

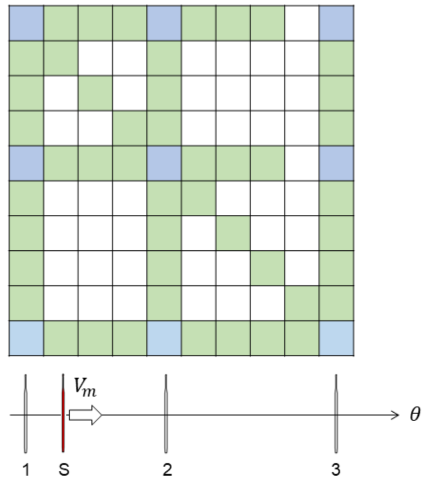

Fig. 5 Cross-Spectral Matrix for an array with three fixed microphones and one scanning sensor. The contributions from the fixed and scanning microphones are highlighted in blue and green, respectively. The polar angle is displayed as θ.

where $J = \left(\mathcal{M}_f + K\mathcal{M}_s\right)^2$. Here, the steering vectors are of size $1 \times \left(\mathcal{M}_f + K\mathcal{M}_s\right)$. It is noted that diagonal removal or reconstruction algorithms can be used with the above approach, requiring some modifications on the number of elements J. The steering vector matrix used in Eq. 37 has components associated with both fixed and continuously-scanning sensors. As such, Eq. 2 should used for fixed sensors while Eq. 18 should be used for the components involving scanning sensors. However, Eq. 2 can be used indistinctly as long as certain conditions are met, as discussed in section III.A.

A cautionary comment is noted with regards to the errors associated with the estimation of the missing entries of the CSM, known as Matrix Completion Errors (MCE), and defined as

$$\mathrm{MCE}(\omega) = \frac{\|\mathbf{G}_{\mathrm{real}}(\omega) - \mathbf{G}_C(\omega)\|_F}{\|\mathbf{G}_{\mathrm{real}}(\omega)\|_F} \tag{38}$$

where $\mathbf{G}_{\mathrm{real}}$ is the real global CSM. Past experimental results [27] have measured the performance of the matrix completion error in conjunction with the FISTA algorithm. It is found that the MCE is usually below 0.1 when the signal-to-noise ratio is below 10 dB using exclusively sequential measurements (i.e. without the use of any reference sensors). The MCE improves when utilizing reference sensors and appears independent of the number of references used. As such, FISTA is identified as a robust method of minimizing Eq. 36 when the number of uncorrelated acoustic sources is unknown a priori. No specific trends of the MCE as a function of frequency are noted, as it does not monotonically increase or decrease. The matrix completion problem posed in the present work might be considered as an extension of the FISTA matrix reconstruction problem of Ref. [27], where the reference sensors are the fixed microphones and the sequential measurements are given by the scanning microphone.

C. Partial Fields Decomposition

In line with the previous section, the aim of this section is the construction of a global CSM so that advanced beamforming and deconvolution techniques can be used in conjunction with the continuous-scan paradigm. The approach presented in this section differs from the previous in that there are no elements of the global CSM that are estimated using a minimization algorithm. Instead, this section outlines an approach to construct a global CSM using partial fields decomposition (PF). The approach bears similarities to that used by Shah *et al.* [13, 30], and has been successfully applied in the past in the beamforming of fan and jet noise sources [13, 31] and near-field acoustic holography [8, 32, 33]. The method can be considered an extension of the start-and-stop method [8, 32, 33] that relied on having an array of *reference* (fixed) sensors that were measuring simultaneously and continuously while a small subset of the array was scanning over a number of patches sequentially. In this study, the microphone is continuously scanning, and the signal is non-stationary, requiring advanced spectral estimation techniques, as discussed in Section

III.A.

The process involved in obtaining the global CSM with PF decomposition is briefly summarized. First, a reference CSM, denoted by $\mathbf{G}_{ff,T}$ is constructed as

$$\mathbf{G}_{ff,T}(\omega) = G_{f_m f_n,T}(\omega) \;=\; \overline{P_{f_m,T}(\omega)P^*_{f_n,T}(\omega)} \tag{39}$$

The matrix is constructed using the fixed sensors only (indicated by subscripts ff) utilizing the complete pressure time-traces (denoted by subscript T). The reference CSM has a singular value decomposition

$$\mathbf{G}_{ff,T} = \mathbf{U}_{ff,T}\mathbf{\Sigma}_{ff,T}\mathbf{V}^H_{ff,T} \tag{40}$$

The pressure signals from all sensors (fixed and scanning) are then divided into a number K of overlapping or non-overlapping blocks, similarly to the previously-described approaches. A transfer function matrix between the reference microphones and the continuously-scanning sensors is constructed for every block as

$$\mathbf{H}_{fs,k} = \left(\mathbf{G}_{ff,k}\right)^{-1}\mathbf{G}_{fs,k} \tag{41}$$

where $\mathbf{H}_{fs,k}$ represents the transfer function matrix for block k. The term $\mathbf{G}_{ff,k}$ is the CSM calculated utilizing the fixed sensors only for block k, obtained using

$$\mathbf{G}_{ff,k}(\omega) = G_{f_m f_n,k}(\omega) \;=\; \overline{P_{f_m,k}(\omega)P^*_{f_n,k}(\omega)} \tag{42}$$

and $\mathbf{G}_{fs,k}$ is the CSM obtained utilizing the fixed sensors and the scanning microphones, which is computed as

$$\mathbf{G}_{fs,k}(\omega) = G_{f_m s_n,k}(\omega) \;=\; \overline{P_{f_m,k}(\omega)P^*_{s_n,k}(\omega)} \tag{43}$$

The frequency-dependent window is applied in the cross-spectral density estimation of $\mathbf{G}_{fs,k}$. Typically, matrix $\mathbf{G}_{ff,k}$ does not have an inverse. It is a standard procedure to use the Moore-Pensore generalized inverse for the matrix such that

$$\left(\mathbf{G}_{ff,k}\right)^{-1} = \left(\mathbf{G}_{ff,k}\right)^{\dagger} = \mathbf{V}_{ff,k}\mathbf{\Sigma}^{-1}_{ff,k}\mathbf{U}^H_{ff,k} \tag{44}$$

where $\mathbf{G}_{ff,k} = \mathbf{U}_{ff,k}\mathbf{\Sigma}_{ff,k}\mathbf{V}^H_{ff,k}$ is the singular value decomposition of the matrix. The operation $\mathbf{\Sigma}^{-1}_{ff,k}$ is defined as

$$\mathbf{\Sigma}^{-1}_{ff,k} = \begin{pmatrix} \sigma^{-1}_{11} & 0 & \cdots & 0 \\ 0 & \sigma^{-1}_{22} & \cdots & 0 \\ \vdots & \vdots & \ddots & \vdots \\ 0 & 0 & \cdots & \sigma^{-1}_{\mathcal{M}_f\mathcal{M}_f} \end{pmatrix}_k \tag{45}$$

The partial fields for block k are calculated as

$$\mathbf{\Pi}_k = \mathbf{H}^H_{fs,k}\mathbf{U}_{ff,T}\mathbf{\Sigma}^{1/2}_{ff,T} \tag{46}$$

The global CSM is the constructed by "sewing" the partial fields together as [13]

$$\mathbf{G}_{\mathrm{PF}} = \langle \mathbf{\Pi}^H_i \mathbf{\Pi}_j \rangle \tag{47}$$

where $i = 1, ..., K$ and $j = 1, ..., K$. The beamformed image is obtained using the traditional delay-and-sum as

$$Y(\xi,\omega) = \frac{1}{J}\sum_{k=1}^{K}\mathbf{e}_k(\xi,\omega)\mathbf{G}_{PF}(\omega)\,\mathbf{e}^H_k(\xi,\omega) \tag{48}$$

In line with the previous section, diagonal removal or diagonal reconstruction algorithms can be used, the first requiring a change in the number of elements J. The steering vector matrix used in Eq. 48, of size $1 \times K\mathcal{M}_s$, has components associated with continuously-scanning sensors (i.e. the different blocks at which the PF are calculated). Similarly as in the previous section, Eq. 2 can be used to form all the steering vectors if $\omega_{mk} \approx \omega'_{mk}$.

Care must be taken when interpreting the results obtained with PF decomposition. The partial fields are constructed by using phase information from the *reference* sensors. As such, a sufficiently large number of fixed microphones is needed to obtain an accurate representation of the acoustic sources. The number of uncorrelated sources for a given experiment can be determined by calculating the singular values of the reference cross-spectral matrix. By analyzing the relative difference between the most dominant singular values for a given frequency, one might notice that the acoustic field might be represented by a certain number of uncorrelated sources. For the case of the jet noise source presented in this work, it is expected that the ranked singular values of the reference CSM are well separated at low frequencies, where large scale turbulence structures dominate the noise production. The differences between the distinct singular values are expected to decrease as the frequency increases, a manifestation of the randomness of the noise generation due to the fine scale turbulence structures. As such, the PF results will be more accurate at low and mid frequencies. Luckily, the frequencies of interest for this work are well-represented using a reduced number of uncorrelated sources (see Fig. 14).

D. Deconvolution Methods

In traditional beamforming, including its extensions to the continuous-scan paradigm, the array response $Y(x,\omega)$ is the convolution between the point spread function (PSF) and the source distribution, which is written as

$$Y(x,\omega) = \int S(\xi,x,\omega)\Phi(\xi,\omega)dx \tag{49}$$

Here $\Phi(\xi,\omega)$ is the unknown source distribution that causes the beamformed map $Y(x,\omega)$, and $S(\xi,x,\omega)$ is the PSF. Some studies approximate Eq. 49 by using a shift-invariant PSF (i.e. $S(x,\xi,\omega) = S(x-\xi,\omega)$). However, such approximation is only valid when the source is sufficiently far from the microphone array, a condition that is not usually fulfilled in acoustic beamforming applications. Thus, no assumptions with regards to the PSF are made in this study, which increases the computational cost of obtaining the source distribution but also enhances its spatial resolution.

Several deconvolution approaches have been proposed to improve the spatial resolution of the image and reject the sidelobes that are inherent in the PSF. This study explored three of such methods: DAMAS [4], Clean-SC [5] and the Richardson-Lucy (R-L) algorithm [3, 34–36]. The DAMAS and Clean-SC deconvolution processes are implemented as in Refs. [4] and [5], respetively. Both methods require a global CSM, hence they cannot be used for deconvolving the images obtained with CSDAS. In obtaining the modeled or degraded CSMs when using DAMAS or Clean-SC, respectively, one might encounter steering vectors associated with fixed and scanning sensors. As such, Eqs. 2 and 18 should be used depending on whether the sensor is fixed or scanning, respectively. However, Eq. 2 was used independently given the low scanning sensor speed, as detailed in Section III.A.

While the DAMAS algorithm assumes the sources to be statistically uncorrelated, which might not be true in many aeroacoustic applications, the Clean-SC method does not make an assumption with regards to the sources. Rather, Clean-SC is based on the fact that the sidelobes are coherent with the main beam lobe, and removes their contributions iteratively from the noise source maps. In doing so, the contributions from the peak sources are removed from the global CSM, thus forming a degraded version of the matrix. The process stops when the CSM is sufficiently degraded. Clean-SC might have difficulties when localizing a high number of spatially incoherent sources, tending to merge closely-spaced sources into a single source of higher intensity [37].

The Richardson-Lucy image restoration algorithm is briefly described next. The technique has been extensively used in astronomy [38] and acoustic beamforming in the past [3, 9, 19, 36], and is based on assigning the meaning of a conditional probability to the PSF. The inversion method uses Bayes' theorem to find the inverse conditional probability $S(\xi|x,\omega)$. The R-L deconvolution presents some advantages when compared to DAMAS and Clean-SC, as one only needs the PSF to obtain the deconvolved source distribution. Thus, the R-L method can be applied to the CSDAS approach. Similarly to DAMAS, the R-L deconvolution assumes the sources to be statistically incoherent. A method similar to that of Ref. [3] is used in obtaining $\Phi(\xi,\omega)$. For a given frequency, and assuming a total of N incoherent sources, Eq. 49 is discretized as

$$\begin{aligned}
&Y(x,\omega) \rightarrow Y_i \\
&S(x,\xi,\omega) \rightarrow S_{ni} \\
&\Phi(\xi,\omega)\Delta\xi \rightarrow \Phi_n
\end{aligned}$$

such that the following linear system is obtained

$$Y_i = \sum_{n=1}^{N} S_{in} \Phi_n \tag{50}$$

The Richardson-Lucy iteration algorithm is

$$\Phi_n^{(r)} = \Phi_n^{(r-1)} \frac{1}{\sum_{i=1}^{N} S_{in}} \sum_{i=1}^{N} \frac{S_{in} Y_i}{\tilde{Y}_i} \tag{51}$$

where r denotes the iteration step and

$$\tilde{Y}_i = \sum_{n=1}^{N} S_{in} \Phi_n^{(r-1)} \tag{52}$$

The Richardson-Lucy image restoration technique produces similar results to those obtained using DAMAS [19].

IV. Experimental Setup

A. Noise Sources

This study examined two noise sources: a synthetic source distribution and an underexpanded screeching jet. The synthetic noise source was created using a distribution of uncorrelated monopoles without any noise addition, and all of them having equal strength. The pressure field due to the presence of the distributed sources was propagated in the time domain at all fixed and scanning microphone positions, shown in Fig. 8. The position of the scanning microphone was determined from the encoder signal of the motor used in the underexpanded jet experiments. A sampling frequency of 250 kHz and 12 seconds of recording time were used.

The supersonic jet issued from a convergent round nozzle with exit diameter $D = 14.22$ mm and lip thickness of 0.4 mm, shown in Fig. 6. The nozzle was supplied by air at room temperature and pressure of $p_0 = 297$ kPa, with p_0 used for stagnation pressure. This resulted in a fully-expanded jet Mach number of $M_j = 1.34$, with corresponding fully-expanded velocity of $U_j = 397$ m/s. At such conditions, the jet emitted strong screech tones, and oscillated in a lateral fashion (mode B). This source was selected due to the richness of the far-field acoustic components, including the turbulence mixing noise, broadband shock-associated noise and screech tones. In addition to the isolated jet, a conical reflector surface was mounted near the nozzle exit. The structure had a base diameter of $4.22D$ and its cone half-angle was 60°. The presence of the reflector changed the feedback mechanism loop and induced new jet screech modes [39]. Structures upstream of the nozzle were covered with anechoic foam to minimize any reflections towards the nozzle.

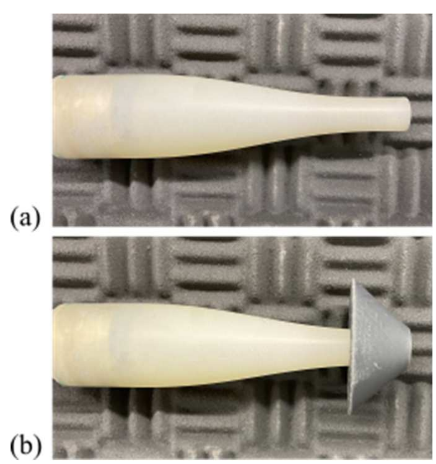

Fig. 6 Photographs of the nozzle (a) and the 60° conical reflector (b).

The Reynolds number based on nozzle exit diameter was 6.5×10^5 for the above conditions. During each experimental run, the total pressure was held to within 1% of its target value.

B. Phased Microphone Array

Noise measurements were conducted in the UCI Aeroacoustics Facility depicted in Fig. 7. The microphone array comprises twenty-four 1/8-inch condenser microphones (Brüel and Kjaer, Model 4138) with frequency response up to 120 kHz. The microphones are connected, in groups of four, to six conditioning amplifiers (Brüel and Kjaer, Model 2690-A-0S4). The outputs of the amplifiers are sampled simultaneously, at 250 kHz per channel, by three 8-channel multi-function data acquisition boards (National Instruments PCI-6143) installed in a computer with an Intel i7-7700K quad-core processor. National Instruments Labview software provides the interface for signal acquisition and filtering, as well as control of the experiment. The microphone signals were conditioned with a high-pass filter set at 350 Hz to remove any spurious noise. Temperature and humidity inside the chamber were recorded to enable the calculation of the effects of atmospheric absorption.

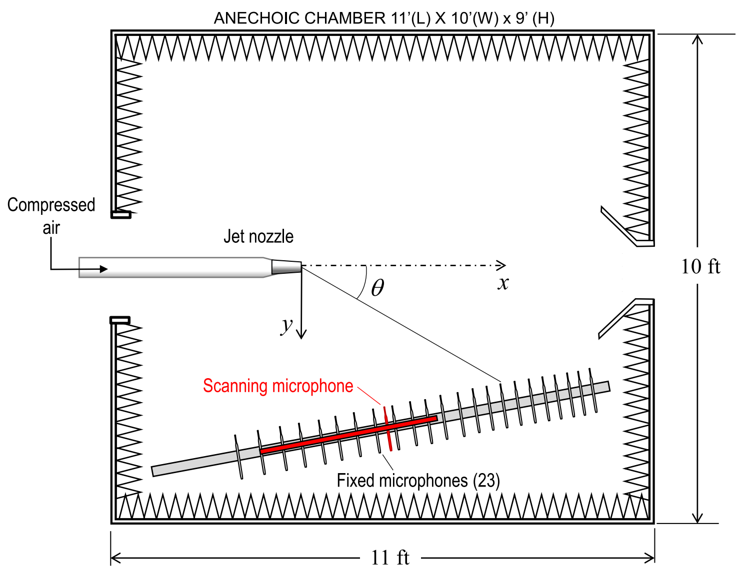

Fig. 7 Diagram of the UCI anechoic chamber. The scanning microphone is indicated in red.

Far-field noise measurements were conducted with the microphones mounted on a linear inclined holder and covering a polar aperture from $\theta = 19°$ to $101°$, with the polar angle θ measured from the jet centerline with reference the nozzle exit (see Fig. 7). The minimum distance from the nozzle exit was $R = 0.9$ m. Twenty-three microphones were fixed and one was scanning continuously along a line very close to the line of the fixed sensors. The scanning microphone was mounted on a linear traverse consisting of a belt drive (Igus ZLW-0630) powered by a servo motor (ClearPath MCPV). The trajectory of the scanning microphone was parallel to the fixed microphone line, with a lateral offset $\Delta z = -6$ mm. The position of the scanning microphone was determined from the encoder signal of the motor (ClearPath MCPV) powering the traverse and verified by a laser displacement sensor (SICK OD1000). The servo was programmed to rotate at fixed revolutions per minute with a velocity ramp-up and ramp-down to prevent damage to the scanning microphone. The steady-state speed was of 75.94 mm/s, with a stroke length of 900 mm. A total of 3×10^6 samples were acquired for each channel, corresponding to an acquisition time of 12 s. Further details on the scanning microphone setup can be found in Ref. [9].

Sound Pressure Level (SPL) spectra were computed from the microphone signals using a Fast Fourier Transform (FFT) size of 4096, giving a frequency resolution of 61 Hz. The SPL spectra were corrected for actuator response, microphone free-field response, and atmospheric absorption. They are referenced to a constant radius of 0.305 m from the nozzle exit.

The beamforming results presented here utilized only thirteen of the fixed microphones ($\mathcal{M}_f = 13$) in combination with the scanning microphone($\mathcal{M}_s = 1$), as shown in Fig. 8. This arrangement covered the polar sector $55 \le \theta \le 101°$,

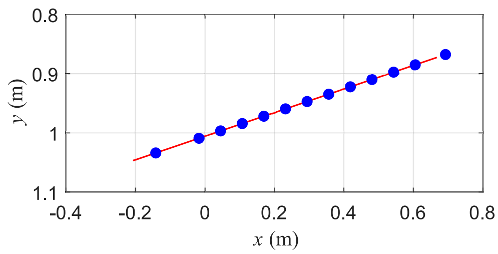

Fig. 8 Fixed microphone coordinates (blue) and scanned region (red).

which is relevant to the screech emission of the jet flows considered here. Noise source maps computed using the thirteen fixed sensors only are also included for reference. The signal was divided into a total of $K = 352$ blocks (excluding block 0 for the CSDAS approach), following the signal division guidance of Ref. [12]. The block schedule utilized a block size of 32768 samples, corresponding to 0.13 s and a traversed length of approximately 10 mm. The block overlap was approximately 50%. The window parameter c_λ was 0.2. The region of interest was set to $-0.3 \leq x \leq 0.65$, or $-22 \leq x/D \leq 46$. In using the DAS algorithm, the region of interest was divided into 350 points, thus yielding a resolution of $\Delta x = 2.7$ mm $= 0.2D$. The guidance from Ref. [4] was used for the deconvolution approaches to avoid spatial aliasing problems. Specifically, the ratio $\Delta x / B_{\text{-3 dB}}$ was kept approximately constant and equal to 0.2, where $B_{\text{-3 dB}}$ is the main lobe beam width (-3 dB cutoff beam width) taken at $x = 0$ m. This lead to a frequency-dependent number of divisions of the region of interest, rapidly increasing with frequency. To limit the computational cost of the inversion process, the maximum number of grid points at high frequency was capped at 350, thus yielding a maximum spatial resolution of $\Delta x = 2.7$ mm $= 0.2D$. The maximum error for DAMAS and the R-L methods was set to 0.1, being defined as

$$r = \frac{|\mathbf{Y} - \mathbf{S}\mathbf{\Phi}|}{|\mathbf{Y}|}$$

The stopping criterion for the Clean-SC deconvolution was

$$\|\mathbf{G}_{\text{degraded}}\|_F > \|\mathbf{G}\|_F$$

C. Array Pattern

The array point spread function (Eq. 49) affects the spatial resolution of the beamformed images. The PSF measures the performance of the microphone array in the presence of a localized point source (i.e., a monopole). Ideally, the array responds to such source by showing a highly-localized peak in the noise source map, without the presence of any artificial and secondary sources. However, the sharpness of the noise source map and the appearance of the so-called ghost sources are inherent to the geometrical deployment of the array and its PSF. Thus, the beamformed maps ($Y(\xi, \omega)$) might not truly represent the source distribution. Past research has been conducted on optimizing the array geometry to improve the spatial resolution of the beamformed images [1, 40, 41]. However, the sidelobes can only be suppressed to a certain extent.

The continuous-scan paradigm reduces the sidelobe levels significantly. The reduction is obviously dependent on the block schedule that is utilized (e.g., a relatively coarse block distribution will not suppress the sidelobes as much as a fine distribution). The PSFs of the continuous-scan approaches of this work are studied next.

The PSF is usually characterized by the main lobe beam width and the relative sidelobe level. With regards to the main lobe beam width, it is found to be inversely proportional to frequency $B_{-3\text{dB}} \approx CR/(fD)$, where D is the aperture of the array, R is the average distance between the array and the measurement plane, and C is an experimentally-found constant [4]. In this study, $D = 0.85$ m, $R = 1.02$ m and $C = 308.34$. The constants are similar for the all array configurations used in this work as the aperture has been kept approximately the same for all the noise source maps. The relative sidelobe level is shown in Fig. 9. The image displays the PSF for a point source at $x = 0$ m, calculated using the various continuous-scan methodologies. For reference, the PSF calculated using the fixed sensors only is also included. The PSF of the CSMC method was virtually identical to that of the PF decomposition and was not included. The figure demonstrates how the continuous-scan approach suppresses the sidelobe levels to a great extent compared to using the fixed sensors only. It is thus expected that the continuous-scan beamformed maps will present a higher spatial resolution and higher fidelity in imaging the noise sources.

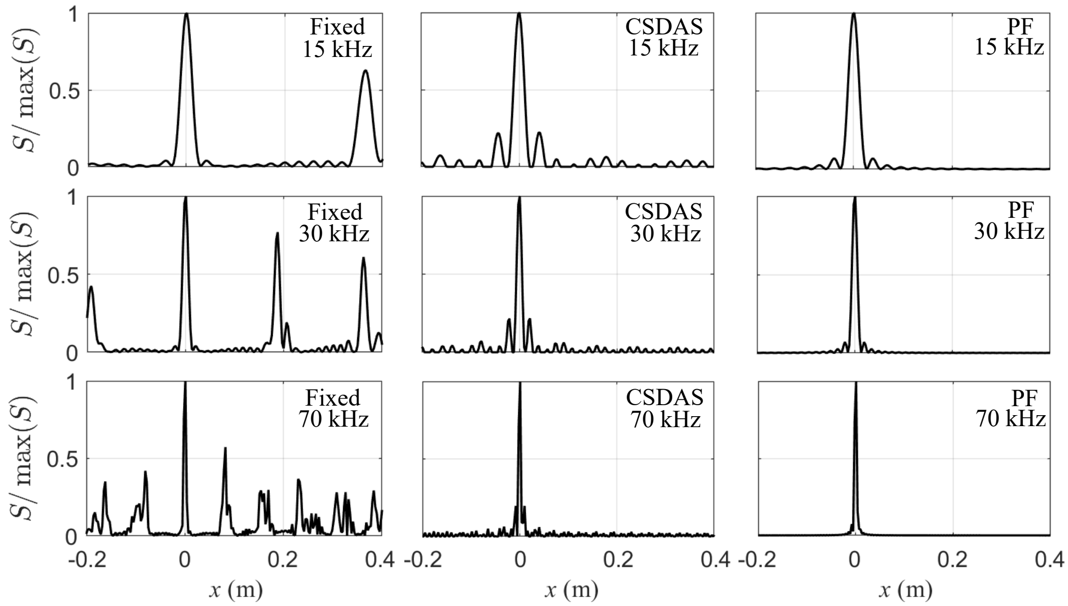

Fig. 9 Normalized point spread function for a source at $x = 0$ for three frequencies. Left column: fixed sensors only; middle column: CSDAS; right column: Partial-field decomposition.

V. Results

A. Synthetic Noise Source

With the aim of quantifying the performance of the three continuous-scan methodologies introduced, a synthetic uncorrelated distributed noise source was simulated. The simulated source conforms the University of California, Irvine acronym, UCI, as depicted in Fig. 10. The beamformed and deconvolved contour plots are used as a benchmark in assessing the spatial resolution of the continuous-scan approaches.

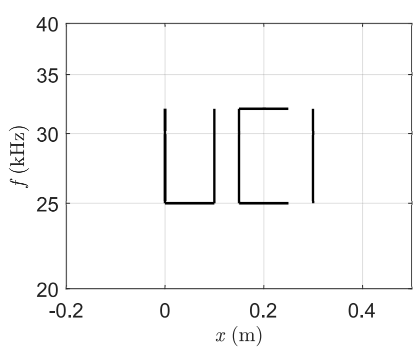

Fig. 10 Synthetic distributed uncorrelated noise source.

Beamformed maps computed using DAS are presented in Fig. 11. A dynamic range of 20 dB is used, with the local maximum is set to 0 dB. For the CSDAS and PF-DAS methods the diagonal of the CSMs was optimized using the previously described DiRec method. The DAS with fixed sensors clearly fails to resolve the source: the number of microphones is insufficient to correctly determine the spatial distribution of the source and ghost sources appear. The image is significantly improved when utilizing the CSDAS approach, reducing the presence of ghost sources. Application of the PF-DAS or CSMC-DAS greatly improves the quality of the results, reducing the effect of the sidelobes and resulting in a sharply localized source. It is seen how the maps obtained with the PF and CSMC approaches are of similar quality.

The source distribution can be further sharpened using a deconvolution approach such as DAMAS. This is done in Fig. 12. The distribution obtained using the CSDAS approach cannot be deconvolved using DAMAS due to the lack of a global CSM, as discussed in previous sections.

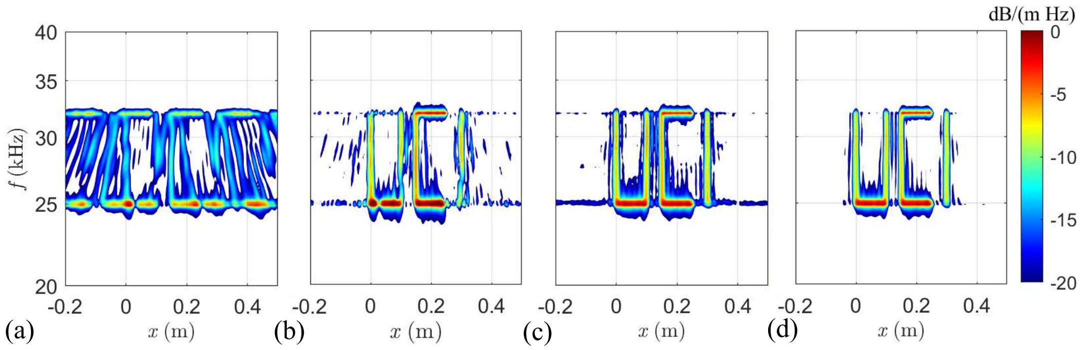

Fig. 11 DAS beamforming results for the synthetic distributed uncorrelated source. (a) Fixed sensors only; (b) CSDAS; (c) PF - DAS; (d) CSMC - DAS.

Deconvolution using the fixed sensors only fails to provide any meaningful information about the spatial distribution of the source. This is caused by the input image being significantly distorted, which impairs the deconvolution process. On the other hand, both the PF and CSMC approaches result in images that are very sharp, with the source being almost perfectly localized, and without the presence of ghost sources. Figures 11 and 12 demonstrate the ability of the methodologies presented in this study to obtain well-resolved images, even with relatively sparse microphone arrays.

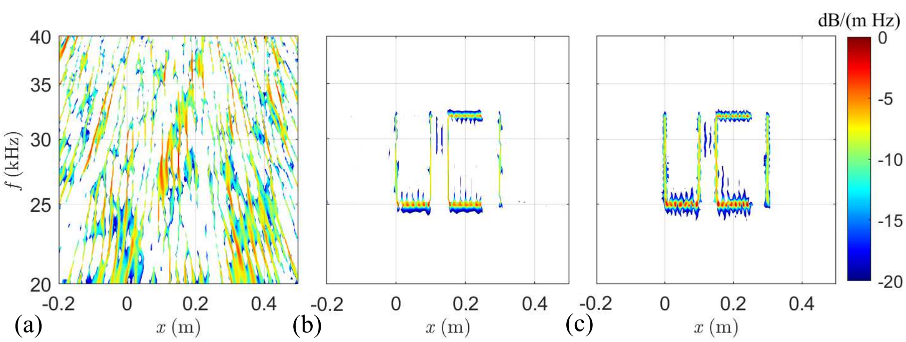

Fig. 12 DAMAS results for the synthetic distributed uncorrelated source. (a) Fixed sensors only; (b) PF - DAMAS; (c) CSMC - DAMAS.

B. Jet Noise Source

This section presents the SPL spectra and noise source distributions for the two jet configurations used in this work. SPL spectra are presented based on the full record of the microphone signals (12 seconds). They are plotted for several polar angle stations, at which one encounters a richness of tones. In the presentation of the results the notation $X^{(n)}$ is used to designate a screech tone, where X is the mode and n is the harmonic. The mode notation of Ref. [42] is followed, with mode B denoting a lateral oscillation. The jet configuration with the 60° reflector contained an "unknown" mode, denoted as mode E in Ref [39]. Its jet oscillation dynamics are not known, and additional near-field data would be required to fully characterize it. Tone F, which appeared to be the complex interaction between two modes, appeared for the reflector configuration. Its frequency follows $f_{F^{(1)}} \approx f_{B^{(1)}} + f_{E^{(1)}}$.

Figure 13 displays the lossless SPL spectra for the isolated jet (black) and the jet with the 60° reflector (red). Tones $B^{(1)}$, $B^{(2)}$, $B^{(3)}$ and $B^{(4)}$ appear very prominently for the isolated jet. Their directivity is not uniform, hence their levels vary depending on the polar station [43, 44]. The effect of the 60° reflector is clear from the figures. Tones $E^{(1)}$, $E^{(2)}$ and $F^{(1)}$ arise, with tone $E^{(1)}$ dominating all the covered polar angles. Note that the 60° reflector suppresses the peak tone level at high polar stations, and is also associated with a decrease of the broadband shock-associated noise. It was found in Ref. [39] that modes B and E were coexisting, and no mode switching for the 60° configuration was noted.

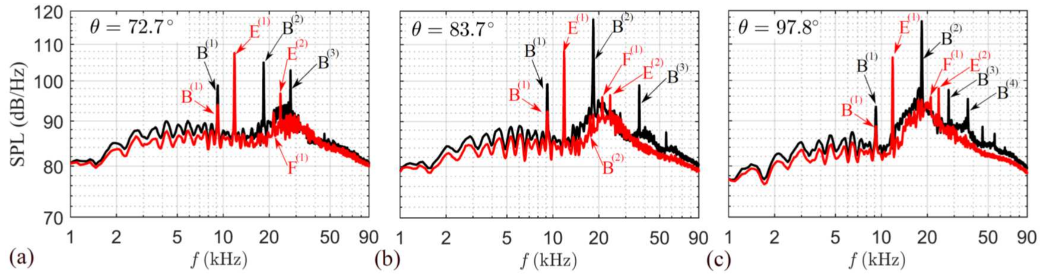

Fig. 13 SPL spectra for the isolate jet (black) and the jet with the 60° **reflector (red) at different polar angles. (a)** θ = 72.7°**; (b)** θ = 83.7°**; and (c)** θ = 97.8°

The beamforming results are obtained using the fixed sensors and the three continuous-scan methodologies presented in this work. The MCE for the CSMC method cannot be computed for the jet experiments due to the lack of a global CSM. However, the results from PF and CSMC were of similar quality. Thus deconvolution for the global noise source maps has been mainly carried out using the PF decomposition technique, as its validity can be rapidly assessed. Figure 14 shows the singular values of the diagonal of $\mathbf{\Sigma}_{ff,T}$, calculated using Eq. 40, for the isolated underexpanded jet. The values are plotted against the frequency range of interest. The size of the $\mathbf{\Sigma}_{ff,T}$ matrix is of 13 × 13 and only the odd-numbered entries of the diagonal are displayed in the figure. It can be seen that there is a relatively good separation between the largest and the smallest singular values for frequencies up to 50 kHz, suggesting that the majority of the energy for such frequency range can be described utilizing a reduced number of independent sources. The opposite behavior is observed for frequencies larger than 50 kHz. The screech tone and its harmonics appear to be well represented using one to three distinct sources. A similar behavior is noted for the jet with the 60° reflector. Thus, it is expected that the beamforming results presented in this work will be more accurate for the frequency range of $1 \leq f \leq 50$ kHz, and start degrading for $f > 50$ kHz. This is true for the PF decomposition and CSMC techniques.

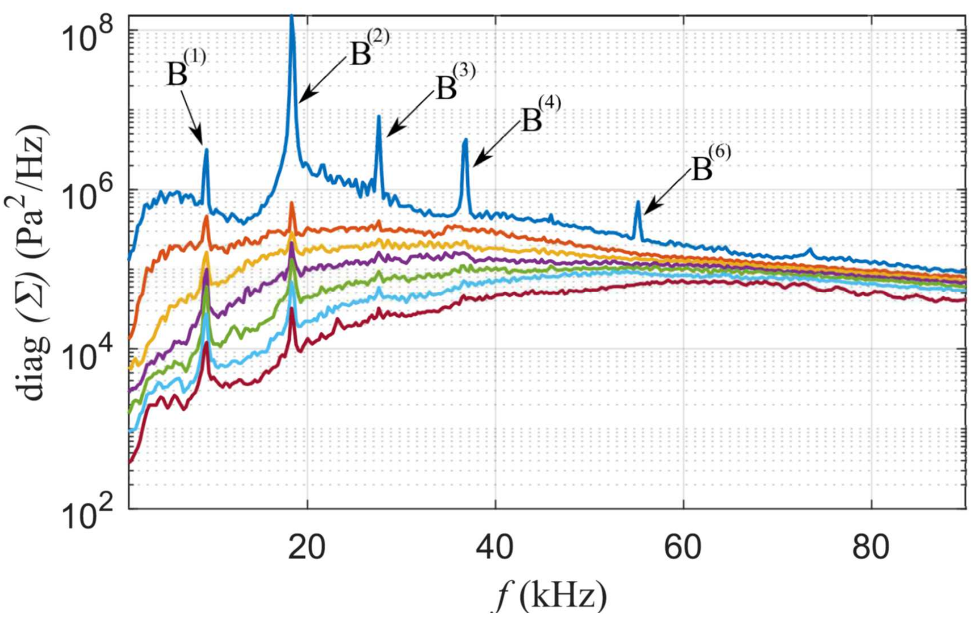

Fig. 14 Ranked odd-numbered singular values from matrix $\mathbf{\Sigma}_{ff,T}$ for the isolated supersonic jet.

1. Isolated Jet

Beamforming results for the isolated jet are shown in Fig. 15. The signal treatment is the same as that discussed in conjunction with Fig. 11. The noise source map obtained with fixed sensors only lacks of the spatial resolution needed for aeroacoustic applications. The source distribution at high frequency is greatly contaminated by the sidelobes and no useful information can be extracted. This is due to the combination of a relatively sparse microphone array and a sensor deployment that has not been optimized to reduce the sidelobes. The continuous-scan paradigm greatly increases the resolution of the beamformed maps, as demonstrated by earlier works [9, 13, 30, 39]. It is seen how the CSDAS, PF-DAS and CSMC-DAS methods produce maps of similar quality and are practically devoid of any sidelobe contamination.

The source appears to cover many nozzle diameters (up to $x = 0.3$ m $\approx 20D$) at low frequency, whereas it is closer to the nozzle exit at high frequency. This behavior has been seen in past works [9, 13, 39]. The jet nozzle exit is located approximately at $x = 0$ m. The horizontal thin layers containing periodic-like patterns represent the location of screech tones $B^{(1)}$, $B^{(2)}$, $B^{(3)}$, and $B^{(4)}$. A weak source around $x = 0$ m is seen near 9 kHz in the continuous-scan maps, indicating the interaction of upstream-propagating waves of tone $B^{(1)}$ with the nozzle lip. This effect is impossible to discern using the fixed sensors only. At a frequency range of $30 \leq f \leq 50$ kHz, periodic vertical streaks can be discerned with the three continuous-scan methods. They are discernible to about $x = 0.1$ m $\approx 7D$. These "shock sources" are associated with the turbulence convected downstream and its interaction with the shock cell structure of the jet, and are approximately aligned with the shock-cells of the jet flow [45]. The continuous-scan approach reduces the need for deconvolution as the DAS maps are already free of ghost sources. However, deconvolution approaches might still be applied to further sharpen the noise source distributions. This is done in Fig. 16. For the results that follow, the contour plots obtained using the fixed sensors only are omitted due to their low spatial resolution.

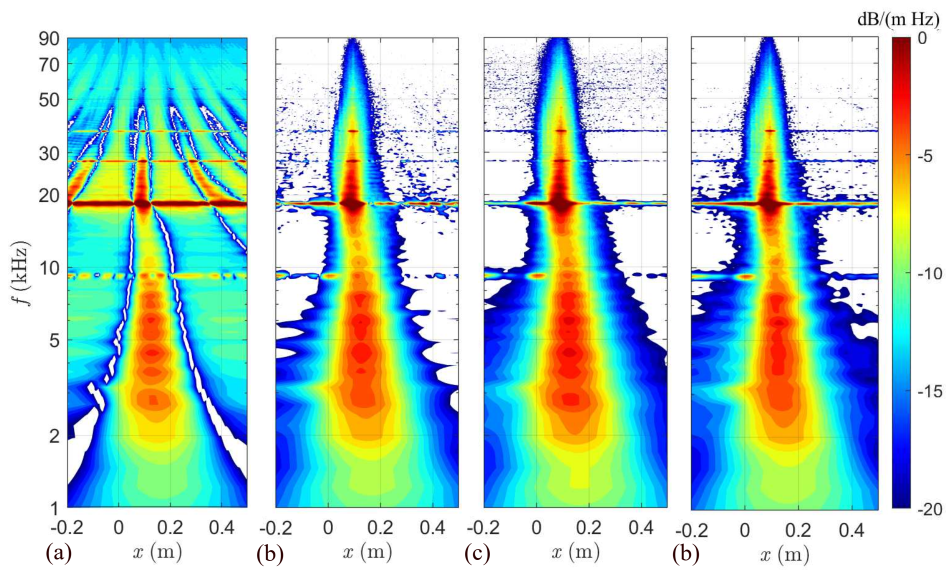

Fig. 15 Beamformed maps of the isolated supersonic jet obtained with DAS using different methods. (a) FRDAS; (b) CSDAS; (c) PF; (d) CSMC.

Figure 16 presents the results for DAMAS, R-L and Clean-SC deconvolution algorithms of the DAS array responses obtained with PF decomposition. The CSMC deconvolution results were of similar quality and will be only used in assessing the shock sources. The deconvolved noise source maps are obviously of higher quality to those obtained with DAS only. The source becomes highly localized and the small-scale spatial features of the jet flow are very well-resolved. It is instructive to examine the source distribution around tones $B^{(1)}$, $B^{(2)}$, $B^{(3)}$ and $B^{(4)}$, marked with horizontal lines in the DAMAS map. The source distribution near the $B^{(1)}$ frequency appears to have some periodicity when deconvolved using DAMAS. However, this effect is not seen when using the R-L deconvolution or Clean-SC. The strong reflection from the nozzle lip near $x = 0$ m, associated with the upstream-propagating waves of tone $B^{(1)}$ that close the feedback mechanism loop, is clearly visible. Reflections from the nozzle lip can also be seen for tone

$B^{(2)}$, a behavior not seen in the beamformed maps of Ref. [39], underscoring the complexity of the screech problem. The location of the source peak for tones $B^{(2)}$, $B^{(3)}$ and $B^{(4)}$ is between $0.084 \leq x \leq 0.088$ m, corresponding to $5.9 \leq x/D \leq 6.25$. This apparent location is $1D$ downstream of the location from which the upstream-travelling waves were identified to be originated from for mode B by Powell *et al.* [46], and Mercier *et al.* [47], but is in line with previous experimental beamforming results of Ref. [39].

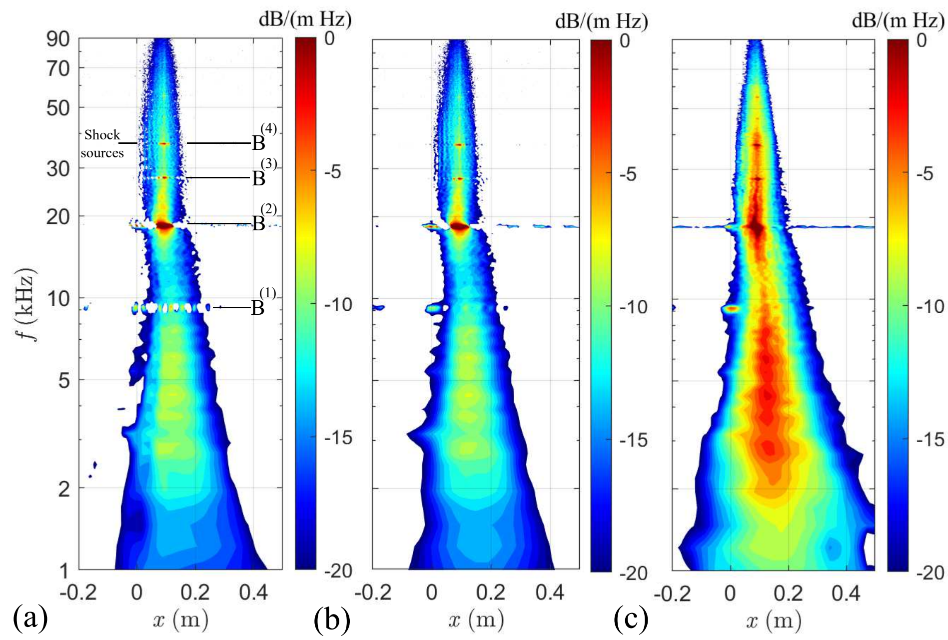

Fig. 16 Deconvolved noise source maps obtained with PF using different algorithms: (a) DAMAS; (b) R-L; (c) Clean-SC.

The spatial pattern associated with the shock-cell structures near $30 \leq f \leq 50$ kHz is further explored in Fig. 17. A dynamic range of 12 dB is used, and the local maximum is set to 0 dB. The image displays a detail of the noise source map obtained with PF (a and c) and CSMC (b and d) using the R-L deconvolution (a and b) and DAMAS (c and d). Moderate averaging in frequency, with a window of ~ 1 kHz, was used in obtaining the contour maps to remove the effects of spurious wiggles in the source distribution. The black dashed vertical lines display the approximate location of the peak source, obtained by finding the local maxima near $35 \leq f \leq 45$ kHz. The figure demonstrates how the location of the shock sources is largely independent of the continuous-scan approach. In addition, it appears that the shock sources are better separated when using the CSMC compared to PF decomposition (notice the difference between the peaks and valleys of the source distribution near the second and third shock sources). It is inferred from the figure that the shock cell spacing, which is approximately the same as the spacing of the shock sources, is between $1.17D$ and $1.20D$. This shock cell spacing, obtained only from the beamforming results, is close to that measured by Mercier *et al.* [47] for a jet at a similar fully-expanded Mach number, obtained through Schlieren visualization analysis. In their study, the shock spacing was near $s = 1.20D$. A similar shock spacing is inferred from the *coherence-based* noise source maps of Ref. [39]. This underscores the high degree of spatial resolution that is attained with the continuous-scan paradigm, independently of the method used, enabling the resolution of the fine scale patterns of the jet flow using far-field non-intrusive measurements. The images deconvolved with Clean-SC have not been included due to the low performance of the method at separating closely-spaced sources [37].

The information drawn from Fig. 17 can be used to predict the screech frequency and determine whether the shock source spacing is physical. In his pioneering work, Powell [48, 49] identified a gain and a phase criteria that must be fulfilled for screech to become self-sustaining. With regards to the gain criterion, he established that the gain associated with all the feedback stages had to be such that amplitude of the new disturbances should at least match that of the previous ones. The phase criterion was formulated in terms of the noise source location ns, the speed of the downstream- and upstream-propagating disturbances (U_1 and U_2, respectively), the frequency $f_{X^{(n)}}$ at which the shear

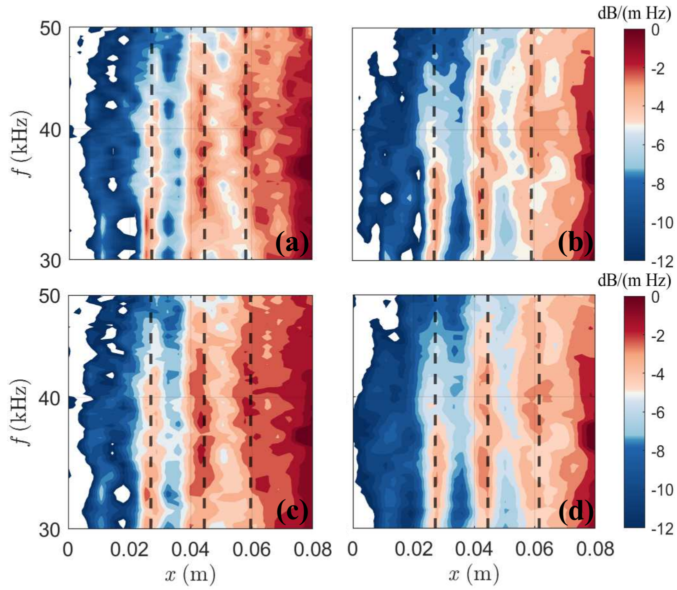

Fig. 17 Detail of the shock cell pattern around tone $B^{(4)}$ of the isolated jet, and position of the shock sources obtained from the DAMAS (c and d) and R-L (a and b) deconvolved images using PF (a and c) and CSMC (b and d).

layer is naturally unstable, and the number of upstream and downstream propagating disturbances N as

$$\frac{N}{f_{X^{(n)}}} = \frac{ns}{U_1} + \frac{ns}{U_2} + \psi \tag{53}$$

where ψ accounts for any delay associated with the receptivity at the nozzle lip or near the reflection surface or with the production of the upstream-propagating wave. Powell originally assumed that screech was generated at one or more of the shocks, and incorporated an additional observation related to the screech directivity to predict its frequency. He modeled the screech tone generation by using a series of phased stationary monopole sources located at the shock tips [48–50]. The screech frequency was predicted based on three monopole sources, connecting the shock spacing and convective Mach number of the downstream-travelling perturbations. By requiring maximum directivity towards the upstream direction ($\theta = 180°$) for the fundamental tone, Powell obtained the well-known relation for the screech frequency

$$f_{X^{(n)}} = \frac{U_c}{s(1 + M_c)} \tag{54}$$

where U_c is the convective velocity, s is the shock spacing, and M_c is the convective Mach number, defined as $Mc = U_c/a_\infty$. Although there are different theories explaining how screech is generated [50, 51], Powell's original relationship is still widely used and provides very accurate predictions of the screech frequency in many operation conditions, including for the lateral oscillation mode studied in this work. Another screech frequency prediction formula, based on the apparent location of the screech source is used. Gao and Li [52] used their numerical data to extract the integer N of concurrent upstream and downstream disturbances used in Powell's general feedback equation (Eq. 53). Based on this, they formulated an equation to predict the screech wavelength

$$\lambda_{X^{(n)}} = \frac{ns}{N}\frac{1 + M_c}{M_c} \tag{55}$$

where $\lambda_{X^{(n)}}$ is the screech wavelength and ns is the effective position of the screech source, that they located at the fifth shock cell. The screech frequency is $f_{X^{(n)}} = a_\infty/\lambda_{X^{(n)}}$. Note that this is similar to Eq. 53 with a time delay or phase lag ψ equal to 0. Gao and Li found that the number of concurrent disturbances N was 5 for jets presenting flapping oscillations (mode B).

We calculate the screech frequency of tone $B^{(1)}$ with Eqs. 54 and 55, using two distinct features of the jet flow extracted from the beamforming results: the spacing of the shock sources and the apparent location of the screech source. Using a convective velocity of $U_c = 0.7U_j$, and a shock spacing of $s \approx 1.18D = 0.0168$ m, obtained from the beamforming results, a screech frequency of $f_s = 9150$ Hz is predicted from Eq. 54. Using Eq. 55 with an approximate screech source location of $x = 6D$, we obtain a screech frequency $f_s = 9000$ Hz. The predicted values deviate less than 2.5% from the measured screech frequency of 9200 Hz. This underscores the high degree of spatial resolution attained with the continuous-scan paradigm and its ability to resolve the very fine details of the jet flow field.

2. Jet with the Reflector Surface

The influence of upstream reflector surfaces on jet screech is studied next. It is widely accepted that the phenomenon of jet resonance is highly dependent on the boundary conditions of the experiment (lip thickness, screech reflection point, etc.). For instance, changes in the lip thickness are associated with a reduction of the screech frequency for mode B, and with higher tone amplitudes when using nozzles with larger lip thicknesses. The modification of the nozzle lip produces changes in the receptivity process, and can even reactivate the screech feedback loop after its cessation [53]. In addition, for a given pressure ratio, the jet might oscillated in a lateral (mode B) or helical fashion (mode C) depending on the nozzle lip thickness. This highly nonlinear behavior is also manifested in the underexpanded jet experiments presented in this work. Here, we used a 60° conical reflection surface to modify the screech feedback loop and infer any changes in the spatial structure of the jet flow using the continuous-scan microphone array.

Figure 18 shows the beamformed maps for the jet with the 60° reflector obtained with DAS, DAMAS and R-L deconvolution using PF decomposition. The overall trends are similar to those of the isolated supersonic jet, with the sources extending further downstream at low frequency and becoming more compact at high frequency. However, some significant differences on the source distributions associated with the screech tones are noted. Similarly as in the previous case, the nozzle exit is located approximately at $x = 0$ m. Screech tones $B^{(1)}$, $B^{(2)}$, $E^{(1)}$, $E^{(2)}$ and $F^{(1)}$, marked in the DAMAS contour plot, can be clearly seen in all the noise source distributions, corresponding to the thin horizontal layers presenting periodic-like patterns for the frequencies between 9 and 25 kHz. Strong reflection sources for tones $B^{(1)}$ and $E^{(1)}$ are seen for x between -0.0216 and -0.018 m, corresponding to $-1.52 \le x/D \le -1.25$. This corresponds approximately to the axial position of the edges of the reflector. Installation of the 60° surface changes the point from which the upstream propagating waves reflect back to the flow, producing changes in the feedback loop length. In addition, it appears that additional upstream-propagating components appear near the frequency range of 12 to 16 kHz when using the reflector surface, a behavior also seen in Ref. [39], and not seen for the isolated supersonic jet. A certain degree of source periodicity is noted near tones $B^{(1)}$ and $E^{(1)}$. The apparent location from which the upstream-traveling waves emanate is not easy to discern and appears to be different for each tone. Tone $E^{(2)}$ is generated near $x = 0.1049$ m $\approx 7.4D$, and tone $F^{(1)}$ near $x = 0.1012$ m $\approx 7.1D$. It is difficult to extract the location of tone $B^{(1)}$ or $B^{(2)}$ from the noise source maps. This is in contrast with the source distribution for the isolated jet (Fig. 16), where the location of the apparent screech source was clearly seen for tones $B^{(2)}$, $B^{(3)}$ and $B^{(4)}$, and a direct manifestation of substantial changes in the jet flow field.

In parallel to the previous analysis, the spatial pattern of the shock-cell structures near $30 \le f \le 50$ kHz is explored in Fig. 19. The figure has been obtained in an analogous manner as Fig. 17. Again, it is seen how the location of the shock sources is largely independent of the continuous-scan approach used. The shock sources appear to be spaced an average distance between $s = 1.16D$ to $1.19D$, which is in line with the isolated jet. The shock spacing was expected to be similar given that it is only a function of the fully-expanded jet Mach number. Powell's formula for the screech frequency (Eq. 54) can be used to predict a screech frequency of tone $B^{(1)}$ near 9100 Hz, similar to the measured frequency. However, the frequency of tone $E^{(1)}$ cannot be predicted using the same equation. In addition, it is difficult to use Eq. 55 to predict the screech frequency of tone $B^{(1)}$ due to the inability to extract the approximate position of the screech source from the beamformed maps. This issue also manifests in the coherence-based noise source maps of Ref. [39]. Regarding tone $E^{(1)}$, Gao and Li's formula does not correctly predict its frequency if one uses that the number of concurrent upstream and downstream disturbances in the jet flow is 5 (i.e. $N = 5$). However, the predicted screech frequency is remarkably close to the measured value (within 1%) if one uses $N = 8$. This might be the case for mode E or might just be a coincidence. Nevertheless, it is reasonable to believe that high screech frequencies are associated with a higher number of concurrent upstream- and downstream-propagating disturbances. For instance, it has been found [52] that jets oscillating in a helical mode are associated with $N = 6$. Thus, given that it is true that $f_{E^{(1)}} > f_{C^{(1)}}$, it is expected that $N_{E^{(1)}} > N_{C^{(1)}}$. Additional near-field data are required to verify and support this statement.

The fact that mode B and mode E have different numbers of concurrent upstream- and downstream-propagating

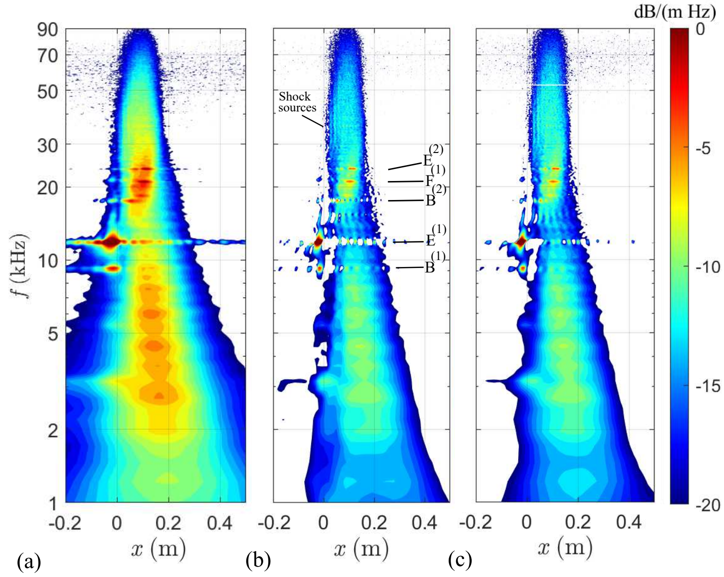

Fig. 18 Noise source maps of the jet with the 60° reflector obtained with: (a) CSDAS; (b) PF - DAMAS; (c) PF - R-L.

waves might also hint at different mechanisms of screech generation. The presence of the upstream reflector appears to produce changes to the jet flow, and the screech modes appear to be very sensitive to such differences. Given that modes B and E were coexisting, it is reasonable to believe that the jet was oscillating in a lateral fashion. It is possible that two mechanisms are at work, exciting the shear layer near $f_{B^{(1)}}$ and $f_{E^{(1)}}$ at the same time, even if the jet is oscillating in a lateral fashion. Shen and Tam [54] suggested that neutral acoustic modes of the jet might also play an important role in the screech process. Similar observation were made by Singh and Chaterjee [55] with regards to oscillation modes A1 and A2. Whether mode E is supported by these neutral acoustic modes cannot be determined from this results alone and is outside the scope of this study.

Sections V.A and V.B reflect the true potential of the continuous-scan paradigm. Its spatial resolution has been assessed using a synthetic noise source and a supersonic underexpanded jet. Empirical and theoretical formulas have been used to predict the screech frequencies, based on distinct features of the jet flow field, with the predictions being within 2.5% of the measured values. In addition to that, it has been found that it is plausible that mode E is associated with $N = 8$ concurrent disturbances, pending additional near-field data for confirmation. The three continuous-scan methods show a remarkable higher level of spatial resolution when compared to the same array using fixed sensors only.

VI. Conclusions

The paper adapted the traditional beamforming methodologies to microphone arrays that include fixed and continuously-scanning sensors. The non-stationarity of the signal introduced by the scanning sensors requires division of the signal into smaller blocks and the application of a frequency-dependent window. The continuous-scan approach also requires a modification of the steering vectors used in traditional beamforming to incorporate a Doppler-shifted frequency when scanning sensors are involved.

Three methodologies are introduced to obtain the noise source maps. The first is a natural extension of the traditional delay-and-sum algorithm to the continuous-scan paradigm. The noise source map is obtained by combining the distinct contributions from the cross-spectral matrices for each block. The method shows highly suppressed sidelobes and an increased spatial resolution compared to an array with fixed sensors only. A cross-spectral matrix completion and a partial fields decomposition method are also introduced. The first technique has been proposed to extend the array resolution from non-synchronous microphone measurements and has been applied to synthetic and industrial noise sources in the past. This paper extends it to the continuous-scan approach. The partial fields decomposition method

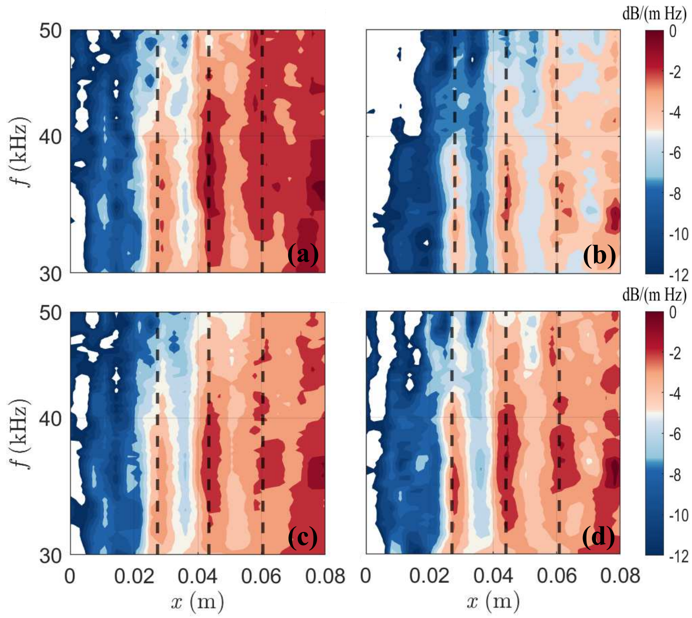

Fig. 19 Detail of the shock cell pattern of the jet with the 60° reflector, and position of the shock sources, obtained from the DAMAS (c and d) and R-L (a and b) deconvolved images using PF (a and c) and CSMC (b and d).

has been used in the past in near-field acoustic holography studies and beamforming. The present work presents a summary of the technique and reformulates it for arrays containing moving sensors. The latter two methods yield noise source maps with very high spatial resolution and almost completely suppressed sidelobes.

The distinct methodologies are validated using a synthetic noise source and are then applied to the acoustic field emitted a supersonic jet that presented the phenomena of screech. It is demonstrated how the very fine details of the source distribution can be resolved with all three methods, enabling to visualize the shock-cell structure of the jet. The shock-cell spacing obtained from the beamformed maps is validated using theoretical and empirical formulas to predict the screech frequency. The screech frequency for mode B is accurately predicted for all the jet configurations.However, the screech frequency for mode E could not be predicted using Powell's original phased monopole source model. A potential distinct mechanism for the generation of mode E has been discussed.

The continuous-scan approach greatly improves the spatial resolution of the imaged noise source, regardless of the method utilized, when compared to a similar array that contains only fixed sensors.

VII. Acknowledgments

This work was supported by Phase II Small Business Innovation Research (SBIR) contract 80NSSC20C0089 under technical monitor Dr. David Stephens of NASA GRC. ATA Engineering, Inc. was the prime.

References

[1] Billingsley, J., and Kinns, R., "The Acoustic Telescope," *Journal of Sound and Vibration*, Vol. 48, No. 4, 1976, pp. 485–510. doi:10.1016/0022-460X(76)90552-6.

[2] Venkatesh, S. R., Polak, D. R., and Narayanan, S., "Beamforming Algorithm for Distributed Source Localization and Its Application to Jet Noise," *AIAA Journal*, Vol. 41, No. 7, 2003, pp. 1238–1246. doi:10.2514/2.2092.

[3] Papamoschou, D., "Imaging of Distributed Directional Noise Sources," *Journal of Sound and Vibration*, Vol. 330, No. 10, 2011, pp. 2265–2280. doi:10.1016/j.jsv.2010.11.025.

[4] Brooks, T. F., and Humphreys, W. M., "A Deconvolution Approach for the Mapping of Acoustic Sources (DAMAS) Determined

from Phased Microphone Arrays," *Journal of Sound and Vibration*, Vol. 294, No. 4, 2006, pp. 856 – 879. doi:10.1016/j.jsv.2005.12.046.

[5] Sijtsma, P., "CLEAN Based on Spatial Source Coherence," *International Journal of Aeroacoustics*, Vol. 6, No. 4, 2007, pp. 357–374. doi:10.1260/147547207783359459.

[6] Dougherty, R., "Extensions of DAMAS and Benefits and Limitations of Deconvolution in Beamforming," *AIAA Paper 2005-2961*, 2005. doi:10.2514/6.2005-2961.

[7] Merino-Martinez, R., Sijtsma, P., Snellen, M., Ahlefeldt, T., Antoni, J., Bahr, C., Blacodon, D., Ernst, D., Finez, A., Funke, S., Geyer, T., Haxter, S., Herold, G., Huang, X., Humphreys, W., Leclere, Q., Malgoezar, A., Michel, U., Padois, T., Pereira, A., Picard, C., Sarradj, E., Siller, J., Simons, D., and Spehr, C., "A Review of Acoustic Imaging Methods Using Phased Microphone Arrays," *CEAS Aeronautical Journal*, Vol. 10, 2019, p. 197–230. doi:10.1007/s13272-019-00383-4.

[8] Lee, M., and Bolton, J. S., "Source Characterization of a Subsonic Jet by Using Near-Field Acoustical Holography," *The Journal of the Acoustical Society of America*, Vol. 121, No. 2, 2007, pp. 967–977. doi:10.1121/1.2404626.

[9] Papamoschou, D., Morata, D., and Shah, P., "Inverse Acoustic Methodology for Continuous-Scan Phased Arrays," *AIAA Journal*, Vol. 57, No. 12, 2019, pp. 5126–5141. doi:10.2514/1.J058085.

[10] Stephens, D. B., and Vold, H., "Order tracking signal processing for open rotor acoustics," *Journal of Sound and Vibration*, Vol. 333, No. 16, 2014, pp. 3818 – 3830. doi:https://doi.org/10.1016/j.jsv.2014.04.005.

[11] Vold, H., Shah, P., Davis, J., Bremner, P., McLaughlin, D., Morris, P., Veltin, J., and McKinley, R., "High Resolution Continuous Scan Acoustical Holography Applied to High-Speed Jet Noise," *AIAA Paper 2010-3754*, 2010. doi:10.2514/6.2010-3754.

[12] Morata, D., and Papamoschou, D., "Advances in the Direct Spectral Estimation of Aeroacoustic Sources Using Continuous-Scan Phased Arrays," *AIAA Paper 2021-0215*, 2021. doi:10.2514/6.2021-0215.

[13] Shah, P. N., White, A., Hensley, D., Papamoschou, D., and Vold, H., "Continuous-Scan Phased Array Measurement Methods for Turbofan Engine Acoustic Testing," *Journal of Engineering for Gas Turbines and Power*, Vol. 141, No. 8, 2019. doi:10.1115/1.4042395.

[14] Nicolas, F., and Rey, M., "S1MAWind Tunnel New Aeroacoustic Capability: a Traversing Microphone Array," *AIAA Paper 2018-3137*, 2018. doi:10.2514/6.2018-3137.

[15] Humphreys, W., Brooks, T., Hunter, W., and Meadows, K., "Design and Use of Microphone Directional Arrays for Aeroacoustic Measurements," *AIAA Paper 1998-471*, 1998. doi:10.2514/6.1998-471.

[16] Amiet, R., "Refraction of Sound by a Shear Layer," *Journal of Sound and Vibration*, Vol. 58, No. 4, 1978, pp. 467–482. doi:10.1016/0022-460X(78)90353-X.

[17] Hald, J., "Cross-Spectral Matrix Diagonal Reconstruction," *Inter-Noise and Noise-Con Conference*, Vol. 253, No. 5, 2016, pp. 3766–3777.

[18] Dougherty, R., "Cross-Spectral Matrix Diagonal Optimization," *Berlin Beamforming Conference (BeBeC)*, 2016.

[19] Ehrenfried, K., and Koop, L., "Comparison of Iterative Deconvolution Algorithms for the Mapping of Acoustic Sources," *AIAA Journal*, Vol. 45, No. 7, 2007, pp. 1584–1595. doi:10.2514/1.26320.

[20] Yu, L., Antoni, J., Wu, H., Leclere, Q., and Jiang, W., "Fast Iteration Algorithms for Implementing the Acoustic Beamforming of Non-Synchronous Measurements," *Mechanical Systems and Signal Processing*, Vol. 134, 2019, p. 106309. doi:10.1016/j.ymssp.2019.106309.

[21] Yu, L., Guo, Q., Chu, N., and Wang, R., "Achieving 3D Beamforming by Non-Synchronous Microphone Array Measurements," *Sensors*, Vol. 20, No. 24, 2020. doi:10.3390/s20247308.

[22] Ning, F., Song, J., Hu, J., and Wei, J., "Sound Source Localization of Non-Synchronous Measurements Beamforming with Block Hermitian Matrix Completion," *Mechanical Systems and Signal Processing*, Vol. 147, 2021, p. 107118. doi:10.1016/j.ymssp.2020.107118.

[23] Hu, D., Ding, J., Zhao, H., and Yu, L., "Spatial Basis Interpretation for Implementing the Acoustic Imaging of Non-Synchronous Measurements," *Applied Acoustics*, Vol. 182, 2021, p. 108198. doi:10.1016/j.apacoust.2021.108198.

[24] Lima Pereira, L. T., Merino-Martínez, R., Ragni, D., Gómez-Ariza, D., and Snellen, M., "Combining Asynchronous Microphone Array Measurements for Enhanced Acoustic Imaging and Volumetric Source Mapping," *Applied Acoustics*, Vol. 182, 2021, p. 108247. doi:10.1016/j.apacoust.2021.108247.

[25] Leclère, Q., "Multi-Channel Spectral Analysis of Multi-Pass Acquisition Measurements," *Mechanical Systems and Signal Processing*, Vol. 23, No. 5, 2009, pp. 1415–1422. doi:10.1016/j.ymssp.2008.12.002.

[26] Yu, L., Antoni, J., and Leclere, Q., "Spectral Matrix Completion by Cyclic Projection and Application to Sound Source Reconstruction from Non-Synchronous Measurements," *Journal of Sound and Vibration*, Vol. 372, 2016, pp. 31–49. doi:10.1016/j.jsv.2016.02.031.

[27] Yu, L., Antoni, J., Leclere, Q., and Jiang, W., "Acoustical Source Reconstruction from Non-Synchronous Sequential Measurements by Fast Iterative Shrinkage Thresholding Algorithm," *Journal of Sound and Vibration*, Vol. 408, 2017, pp. 351–367. doi:10.1016/j.jsv.2017.07.036.

[28] Goates, C. B., Harker, B. M., Neilsen, T. B., and Gee, K. L., "Extending the Bandwidth of an Acoustic Beamforming Array Esing Phase Unwrapping and Array Interpolation," *The Journal of the Acoustical Society of America*, Vol. 141, No. 4, 2017, pp. 407–412. doi:10.1121/1.4981235.

[29] Yu, L., "Acoustical Source Reconstruction from Non-Synchronous Sequential Measurements," *PhD Thesis - INSA de Lyon*, 2015.

[30] Shah, P. N., and Papamoschou, D., "Characterization of High Speed Jet Acoustics Using High-Resolution Multi-Reference Continuous-Scan Acoustic Measurements on a Linear Array," *AIAA Paper 2020-0005*, 2020. doi:10.2514/6.2020-0005.

[31] Lee, A., Shah, P., White, A., Hensley, D., and Schweizer, L., "Continuous-Scan Beamforming for Identification of Highly Varying Amplitude Sources with Low Sensor Budgets," *Berlin Beamforming Conference*, 2020.

[32] Nam, K.-U., and Kim, Y.-H., "A Partial Field Decomposition Algorithm and its Examples for Near-Field Acoustic Holography," *The Journal of the Acoustical Society of America*, Vol. 116, No. 1, 2004, pp. 172–185. doi:10.1121/1.1756896.

[33] Lee, M., and Bolton, J. S., "Scan-Based Near-Field Acoustical Holography and Partial Field Decomposition in the Presence of Noise and Source Level Variation," *The Journal of the Acoustical Society of America*, Vol. 119, No. 1, 2006, pp. 382–393. doi:10.1121/1.2133717.

[34] Richardson, W. H., "Bayesian-Based Iterative Method of Image Restoration," *Journal of the Optical Society of America*, Vol. 62, No. 1, 1972, pp. 55–59. doi:10.1364/JOSA.62.000055.

[35] Lucy, L., "An Iterative Technique for the Rectification of Observed Distributions," *Astronomical Journal*, Vol. 79, 1974, p. 745. doi:10.1086/111605.

[36] Tiana-Roig, E., and Jacobsen, F., "Deconvolution for the Localization of Sound Sources Using a Circular Microphone Array," *The Journal of the Acoustical Society of America*, Vol. 134, No. 3, 2013, pp. 2078–2089. doi:10.1121/1.4816545.

[37] de Santana, L., "Fundamentals of Acoustic Beamforming," *NATO Educational Notes EN-AVT-287-04*, 2017.

[38] Starck, J., Pantin, E., and Murtagh, F., "Deconvolution in Astronomy: A Review," *Publications of the Astronomical Society of the Pacific*, Vol. 144, No. 800, 2002. doi:10.1086/342606.

[39] Morata, D., and Papamoschou, D., "Effect of Nozzle Geometry on the Space-Time Emission of Screech Tones," *AIAA Paper 2021-2306*, 2021. doi:10.2514/6.2021-2306.

[40] Steinberg, B. D., "Principles of Aperture and Array System Design: Including Random and Adaptive Arrays," *New York, Wiley-Interscience*, 1976.

[41] Dougherty, R., "Spiral-Shaped Array for Broad-Band Imaging," *Pat. US 5,838,284*, 1998.

[42] Seiner, J. M., Manning, J. C., and Ponton, M. K., "Dynamic Pressure Loads Associated with Twin Supersonic Plume Resonance," *AIAA Journal*, Vol. 26, No. 8, 1988, pp. 954–960. doi:10.2514/3.9996.

[43] Tam, C. K., Parrish, S. A., and Viswanathan, K., "The Harmonics of Jet Screech Tones," *AIAA Paper 2013-2091*, 2013. doi:10.2514/6.2013-2091.

[44] Norum, T. D., "Screech Suppression in Supersonic Jets," *AIAA Journal*, Vol. 21, No. 2, 1983, pp. 235–240. doi:10.2514/3.8059.

[45] Breen, N. P., and Ahuja, K. K., “Limitations of Acoustic Beamforming for Accurate Jet Noise Source Location,” *AIAA Paper 2020-2603*, 2020. doi:10.2514/6.2020-2603.

[46] Powell, A., Umeda, Y., and Ishii, R., “Observations of the Oscillation Modes of Choked Circular Jets,” *The Journal of the Acoustical Society of America*, Vol. 92, No. 5, 1992, pp. 2823–2836. doi:10.1121/1.404398.

[47] Mercier, B., Castelain, T., and Bailly, C., “Experimental Characterisation of the Screech Feedback Loop in Underexpanded Round Jets,” *Journal of Fluid Mechanics*, Vol. 824, 2017, p. 202–229. doi:10.1017/jfm.2017.336.

[48] Powell, A., “The Noise of Choked Jets,” *The Journal of the Acoustical Society of America*, Vol. 25, No. 3, 1953, pp. 385–389. doi:10.1121/1.1907052.

[49] Powell, A., “On The Mechanism of Choked Jet Noise,” *Proceedings of the Physical Society. Section B*, Vol. 66, No. 12, 1953, pp. 1039–1056. doi:10.1088/0370-1301/66/12/306.

[50] Edgington-Mitchell, D., “Aeroacoustic Resonance and Self-Excitation in Screeching and Impinging Supersonic Jets – A Review,” *International Journal of Aeroacoustics*, Vol. 18, No. 2-3, 2019, pp. 118–188. doi:10.1177/1475472X19834521.

[51] Tam, C., Seiner, J., and Yu, J., “Proposed Relationship Between Broadband Shock Associated Noise and Screech Tones,” *Journal of Sound and Vibration*, Vol. 110, No. 2, 1986, pp. 309–321. doi:10.1016/S0022-460X(86)80212-7.

[52] Gao, J. H., and Li, X. D., “A Multi-Mode Screech Frequency Prediction Formula for Circular Supersonic Jets,” *The Journal of the Acoustical Society of America*, Vol. 127, No. 3, 2010, pp. 1251–1257. doi:10.1121/1.3291001.

[53] Raman, G., “Cessation of Screech in Underexpanded Jets,” *Journal of Fluid Mechanics*, Vol. 336, 1997, p. 69–90. doi: 10.1017/S002211209600451X.

[54] Shen, H., and Tam, C. K. W., “Three-Dimensional Numerical Simulation of the Jet Screech Phenomenon,” *AIAA Journal*, Vol. 40, No. 1, 2002, pp. 33–41. doi:10.2514/2.1638.

[55] Singh, A., and Chaterjee, A., “Numerical Prediction of Supersonic Jet Screech Frequency,” *Shock Waves*, Vol. 17, 2007, p. 263–272. doi:10.1007/s00193-007-0110-1.